

2022-08-01

Thin Film Evaporation Through Engineered Copper Micropillar Arrays

Alejandro Amador
University of Texas at El Paso

Follow this and additional works at: https://scholarworks.utep.edu/open_etd



Part of the [Mechanical Engineering Commons](#)

Recommended Citation

Amador, Alejandro, "Thin Film Evaporation Through Engineered Copper Micropillar Arrays" (2022). *Open Access Theses & Dissertations*. 3584.

https://scholarworks.utep.edu/open_etd/3584

This is brought to you for free and open access by ScholarWorks@UTEP. It has been accepted for inclusion in Open Access Theses & Dissertations by an authorized administrator of ScholarWorks@UTEP. For more information, please contact lweber@utep.edu.

THIN FILM EVAPORATION THROUGH ENGINEERED COPPER MICROPILLAR
ARRAYS

ALEJANDRO AMADOR

Master's Program in Mechanical Engineering

APPROVED:

Md Mahamudur Rahman, Ph.D., Chair

Jack F. Chessa, Ph.D.

Luis R. Contreras Sapien, Ph.D.

Stephen L. Crites, Jr., Ph.D.
Dean of the Graduate School

Copyright ©

by

Alejandro Amador

2022

THIN FILM EVAPORATION THROUGH ENGINEERED COPPER MICROPILLAR
ARRAYS

by

ALEJANDRO AMADOR, B.S.

THESIS

Presented to the Faculty of the Graduate School of

The University of Texas at El Paso

in Partial Fulfillment

of the Requirements

for the Degree of

MASTER OF SCIENCE

Department of Aerospace and Mechanical Engineering

THE UNIVERSITY OF TEXAS AT EL PASO

August 2022

Acknowledgements

Thank you to my family, partner, and friends for all the endless love and support throughout my graduate school studies. My achievements would not be possible without them, and I am truly grateful to have them always pushing me to become a better student and to never stop learning. This would not be possible without all the sacrifice from my parents and everything they have provided me to achieve this level of education.

I would also like to thank my research supervisor, Dr. Md Mahamudur Rahman for all his guidance and support throughout my time as a graduate research assistant at the UTEP Aerospace Center. I am thankful for having such an inspiring and dedicated supervisor that puts student first and engages them to find a true passion for research.

I am grateful for all my colleagues and friends that have I have worked with over the years that have been part of this achievement. A special thanks to Dr. Jason R. Adams for all his expertise and mentorship for this research project. Thank you to Dr. Ahsan Choudhuri for providing me with this opportunity to be involved in such innovating and inspiring research.

Lastly, I would like to thank all UTEP Aerospace Center industry partners for supporting this research and providing endless resources.

Abstract

This work explored and characterized the evaporator section of a fully engineered heat pipe, a proposed semi-passive cooling solution for the thermal management at high heat fluxes, with the use of thin film evaporation. High heat loads present a problem in electronics, circuitry, space, and defense applications which are the main target areas for this cooling solution. Conventionally manufactured flat samples made of copper micropillar arrays were tested to determine their heat removal capabilities for high heat flux applications. The samples were manufactured with 400 μm micropillar hydraulic diameter, various micropillar spacings ranging from 500-1100 μm , with 500 μm and 600 μm micropillar height. These known micropillar dimensions were used to adapt a theoretical model which is used to predict the capillary-limited dry out heat flux. This model considered fluid properties, material properties of the manufactured sample, and micropillar dimensions. The sample's ability for fluid transport and the measure of void spaces throughout this micropillar array were determined for each tested sample based on its micropillar dimensions. Models for these samples were adapted from literature and a relation between micropillar dimensions and theoretically predicted capillary dry-out heat flux was made. Micropillar dimensions are to be optimized to maximize heat removal capacities for these manufactured surfaces for exposure to high temperature and extreme heat fluxes. Higher dry-out heat flux is desired for maximum cooling.

An experimental set up was designed and assembled to test these manufactured test samples using the phase change cooling technique of thin film evaporation with deionized water as the working fluid. This setup was designed to precisely control the flow of deionized water as it enters the manufactured test samples to ensure wicking of the fluid onto the micropillar arrays by capillary action. Pressure and temperature readings were closely monitored to ensure saturation

conditions were present as the tested sample was gradually heated up until dry out is observed. Temperature readings throughout the evaporation assembly were recorded and used to determine the heat flux of the test sample throughout the test. Calculated heat flux was plotted as a function of the temperature difference between the test sample and the saturation temperature.

Various flow rates were tested to determine the point where heat flux becomes independent of flow rate, assuring that dry-out occurred due to high surface temperature and not lack of fluid capillary fluid supply. Manufactured samples made of copper were tested at up to 50 mL/min volumetric flow rate to determine the maximum heat flux they can withstand before dry-out is observed. Samples with the smallest micropillar spacings of 500 μm had the lowest heat flux value of 64.17 W/cm^2 while the manufactured sample having 800 μm spacing dissipated 92.2 W/cm^2 , the most of all samples, showing the most optimized micropillar dimensions of the tested samples. Experimental results were compared with the theoretical model. Experimental results showed good agreement with expected values and showed similar trend as the predicted plot.

Table of Contents

Acknowledgements.....	iv
Abstract.....	v
Table of Contents.....	vii
List of Tables.....	ix
List of Figures.....	x
Chapter 1: Introduction.....	1
1.1 Introduction.....	1
1.2 Phase Change Heat Transfer.....	1
1.3 Thin Film Evaporation.....	2
1.4 Dry-out Heat Flux.....	3
1.5 Motivation.....	3
1.6 Organization of Thesis.....	4
1.7 Statement of Objectives.....	5
Chapter 2: Literature Review.....	6
2.1 Thin Film Evaporation Through Micropillar Wicks.....	6
2.2 Heat Pipe Thermal Management.....	15
Chapter 3: Theoretical Approach.....	20
3.1 Theoretical Approach.....	20
Chapter 4: Experimental Setup.....	24
4.1 Test Facility.....	24
4.1.1 Chamber.....	26
4.1.2 Fluid Canister.....	28
4.1.3 Test Surfaces.....	30
4.1.4 Heater Block.....	34

4.1.5 Data Acquisition System & LabVIEW.....	37
4.2 Test Procedure	37
4.3 Data Processing.....	39
Chapter 5: Thin Film Evaporation Results	41
5.1 Results and Discussion	41
5.1.1 Effect of Flow Rate.....	42
5.1.2 Effect of Micropillar Spacing	43
5.2 Test Summary	45
Chapter 6: Conclusion.....	50
References.....	51
Vita.....	54

List of Tables

Chapter 3

Table 3-1: Fluid properties of water used for calculations. 22

Chapter 4

Table 4-1: Manufactured test sample micropillar dimensions..... 33

List of Figures

Chapter 1

Figure 1-1: Critical heat flux for different cooling solutions. (Zhu 2017)..... 2

Chapter 2

Figure 2-1: Evaporating meniscus regions in thin film evaporation. (Plawsky et al. 2014)..... 7

Figure 2-2: High speed images of the test device during steady-state evaporation at $\approx 20 \text{ W/cm}^2$ and dry out and thermal run away at $\approx 46 \text{ W/cm}^2$ (Solomon et al. 2016) 8

Figure 2-3: Heat flux as a function of temperature difference between the substrate wall and the chamber for device with D, H, and L of 5, 82, and $12 \mu\text{m}$, respectively. (Solomon et al. 2016).... 9

Figure 2-4: Dry out heat flux captured by high-speed camera due to liquid starvation. (Solomon et al. 2016) 10

Figure 2-5: Studied model structures for thin-film evaporation: rectangular ribs (configuration I), vertical square pillars (configuration II), and vertical wires (configuration III). (Farokhnia et al. 2016) 11

Figure 2-6: Interfacial heat flux values predicted compared to experimental measurements for microstructures with varying width to spacing ratios. (Farokhnia et al. 2016) 12

Figure 2-7: Interfacial heat flux values predicted compared to experimental measurements for microstructures with same width to spacing ratios but varying density of pillars. (Farokhnia et al. 2016) 12

Figure 2-8: Variation of base heat flux with meniscus level for various contact angles. (Ranjan et al. 2016) 14

Figure 2-9: Schematic of a heat pipe. (Shukla 2015)..... 16

Figure 2-10: Figure of merit for various heat pipe working fluids. (Chaudhry et al. 2012).....	17
Figure 2-11: Heat pipe wicking limit for various working fluids of proposed wicking surface. (Anderson et al. 2008).....	18
Figure 4-1: CAD of water thin film evaporation test facility.	24

Chapter 4

Figure 4-2: P&ID of thin film evaporation facility.....	25
Figure 4-3: UTEP thin film evaporation test facility.	26
Figure 4-4: Front view of the modular vacuum chamber with attached feedthroughs and flanges.	27
Figure 4-5: Back view of the modular vacuum chamber with attached feedthroughs and flanges.	27
Figure 4-6: Sliced view of evaporation assembly connected inside vacuum chamber.....	28
Figure 4-7: Fluid canister with attached flanges and feedthroughs.	29
Figure 4-8: (a) Primary reservoir with micropillar array. (b) Secondary reservoir.	30
Figure 4-9: (a) Top view of primary reservoir. (b) Bottom view primary reservoir.	31
Figure 4-10: (a) Sliced view of primary reservoir. (b) Sliced view of secondary reservoir.	31
Figure 4-11: Labeled manufactured test sample.	32
Figure 4-12: Labeled micropillar array schematic with micropillar diameter, spacing, and height (a, b, and h).	32
Figure 4-13: SEM images and averaged dimensions for manufacture sample having micropillar dimensions $a=400\mu\text{m}$ $b=500\mu\text{m}$ and $h=500\mu\text{m}$	33

Figure 4-14: SEM images and averaged dimensions for manufacture sample having micropillar dimensions $a=400\mu\text{m}$ $b=500\mu\text{m}$ and $h=600\mu\text{m}$ 33

Figure 4-15: SEM images and averaged dimensions for manufacture sample having micropillar dimensions $a=400\mu\text{m}$ $b=800\mu\text{m}$ and $h=500\mu\text{m}$ 34

Figure 4-16: SEM images and averaged dimensions for manufacture sample having micropillar dimensions $a=400\mu\text{m}$ $b=1100\mu\text{m}$ and $h=500\mu\text{m}$ 34

Figure 4-17: Thin film evaporation assembly with attached test sample. 35

Figure 4-18: Sliced view of the evaporation assembly with attached sample. 35

Figure 4-19: Manufactured cooper heating block..... 36

Figure 4-20: Interior components of the vacuum chamber assembled and connected. 36

Figure 4-21: Thin film evaporation facility LabVIEW display. 37

Figure 4-22: Zoomed view of thermocouple location along the neck of the copper heating block. 39

Chapter 5

Figure 5-1: Theoretically calculated dry-out heat flux for manufactured copper samples..... 41

Figure 5-2: Heat flux as a function of surface superheat at various flow rates for copper sample $a=400\mu\text{m}$ $b=500\mu\text{m}$ $h=600\mu\text{m}$ 43

Figure 5-3: Heat flux as a function of surface superheat for copper samples having $a=400\mu\text{m}$ $h=500\mu\text{m}$ and various spacings at 50 mL/min. 44

Figure 5-4: Theoretical model vs. experimental results for tested copper samples for different contact angles..... 46

Figure 5-5: Experimental results compared to work done by Solomon et al. and Farokhnia et al.

..... 48

Chapter 1: Introduction

1.1 Introduction

High temperature and high heat fluxes present a problem in thermal management which require intricate cooling solutions. Aerospace, defense, and electronics are key areas that are subject to these high heat loads that reduce device performance and cause material degradation. Modern day technology incorporates high performance electronics, high speed vehicles and deep space missions that are subject to very high heat fluxes. It is key to avoid low device performance and avoid failure for constant heat removal of a surface, therefore, different cooling solutions have been proposed for high rates of heat dissipation

1.2 Phase Change Heat Transfer

There exist many different types of cooling solutions nowadays such as single phase and phase change cooling with each having different rates of heat dissipation and heat transfer capabilities. Techniques like pool boiling, flow boiling, and spray cooling all present good thermal management solutions, but each has its downside whether it be fluid transport issues or intricate flow patterns. It is known that the heat transfer coefficient in phase change cooling solutions is higher compared to single phase cooling. Critical heat fluxes for these different types of cooling solutions are shown in Fig. 1-1.

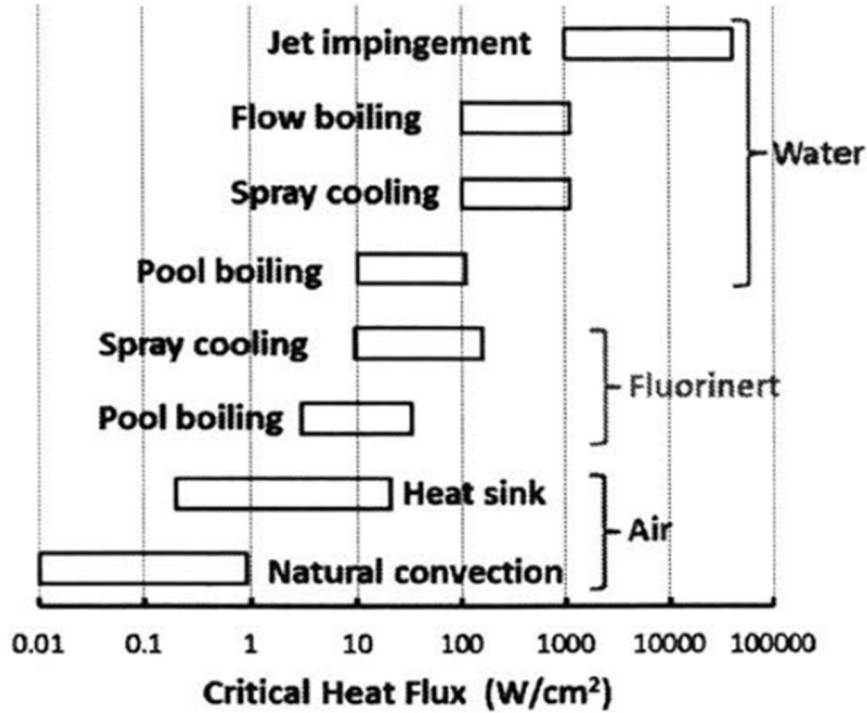


Figure 1-1: Critical heat flux for different cooling solutions. (Zhu 2017)

1.3 Thin Film Evaporation

A phase change cooling strategy that has received a great amount of interest recently is thin film evaporation. This cooling technique relies on the phase change of a thin liquid film of fluid through an extended meniscus which improves thermal transport and rate of heat dissipation by increasing the evaporative area and decreasing the conduction resistance throughout the surface. Evaporative area is increased using micro/nanostructures along a surface which offer high porosity, permeability, and capillary action. Previous thin film studies done by Solomon et al. (2016) have shown that this cooling technique can dissipate very high heat fluxes of up to 6 kW/cm² with microstructure heights in the range of 60-80µm. This cooling technology shows promising heat removal capabilities for small scale, high heat flux applications.

1.4 Dry-out Heat Flux

Dry-out heat flux, often referred to as the critical heat flux, is the maximum heat flux a device can withstand before undergoing failure. Past this point, there will be no heat removal from a targeted surface leading sudden increases in surface temperature that lead to material degradation and failure of these devices. It is essential to determine this critical point for any test device to know its heat transfer capabilities and limits for high heat flux applications. In thin film evaporation, the dry-out heat flux is the point where the working fluid is no longer syphoned or wicked onto the wicking surface due to high surface temperatures leading to a dry-out spot forming furthest away from the liquid supply. This spot rapidly increases radially across the device leading to low performance. This study shows and determines the cooling rates of manufactured test surfaces to determine the effect that micropillar dimensions have on the dry-out heat flux.

1.5 Motivation

The phase change cooling solution of thin evaporation is widely used in heat pipes, a fully sealed cooling device. A heat pipe consists of three sections, an evaporator section, wick section and condenser section and is a fully sealed passive two-phase heat transfer device that takes advantage of a fluids high latent heat of vaporization to achieve efficient heat transfer. Fluid is processed under vacuum conditions which allows for two-phase operations across a wide temperature range. A heat load is inputted into the evaporator section causing the working fluid to boil and transported to the colder region of the heat pipe due to the pressure difference along the device. Vapor gives up latent heat and condenses back into a liquid and absorbed by the wicking structure which passively pumps the fluid back into the evaporator. To characterize and optimize the heat transfer capabilities of this device it is important to experimentally explore the limitations

of each sub-section. Once these sections are characterized and optimized, a fully engineered heat pipe can be designed and manufactured to be incorporated as a cooling solution in high heat flux environments.

This work presented is novel as the team's goal is to explore additively and conventionally manufactured test surfaces for this characterization. Conventionally manufactured copper samples tested in this work incorporated large scale structures for preliminary studies and foundation for future work exploring small scale additively manufactured test surfaces.

1.6 Organization of Thesis

Chapter 1 introduces the fundamentals of thin film evaporation, a phase change cooling solution proposed for high heat flux environments used in a fully sealed passive two phase heat transfer device. Chapter 2 presents studies done and current limitations of this proposed cooling solution. It also discusses how thin film evaporation has been used in copper-water heat pipes and states how this combination is most promising due to fluid and material properties. Chapter 3 presents the theoretical approach taken to create the predicted capillary limited dry-out heat flux plotted against wall-to-wall spacing between micropillars. Chapter 4 focuses the UTEP thin film evaporation test facility, test procedure, and data interpretation steps needed to express the experimental results to detect the dry-out heat flux for each manufactures test sample. Chapter 5 shows the experimental results for each tested sample at a known flow rate and discusses the obtained results and compares them to the theoretical model.

1.7 Statement of Objectives

The goal for this thesis is to design and develop a test facility to study a phase change heat transfer cooling solution for high heat flux environments. Hardware should transport water into a manufactured sample for determining heat transfer capabilities of different manufactured samples.

This thesis outlines the following objectives.

1. Experimentally characterize the evaporator section of a fully engineered heat pipe with the use of thin film evaporation.
2. Experimentally demonstrate the effect of micropillar dimensions on the capillary limited dry-out heat flux.
3. Compare experimental values to literature based theoretical model values.

Chapter 2: Literature Review

2.1 Thin Film Evaporation Through Micropillar Wicks

The phase change heat transfer cooling solution of thin film evaporation has been a very targeted area in research due to its high rates of heat dissipation. This cooling strategy relies on the phase change of a thin liquid film over a surface from an extended meniscus formed by the fluid along a wicking surface. It is important to understand how the working fluid acts when in contact with the substrate surface and how fluid properties affect the rates of heat removal from the surface. For example, solid to liquid interactions like the fluid contact angle on the substrate surface affect the sites of evaporation as attractive forces limit this phase change phenomenon. Capillary pressure and intermolecular forces drive the fluid into the evaporative area where the liquid-vapor interface is less affected by the attraction forces of the solid. Plawsky et al. (2014) describes the regions of thin film evaporation where these different forces interact leading to efficient phase change heat transfer, shown in Fig. 2-1.

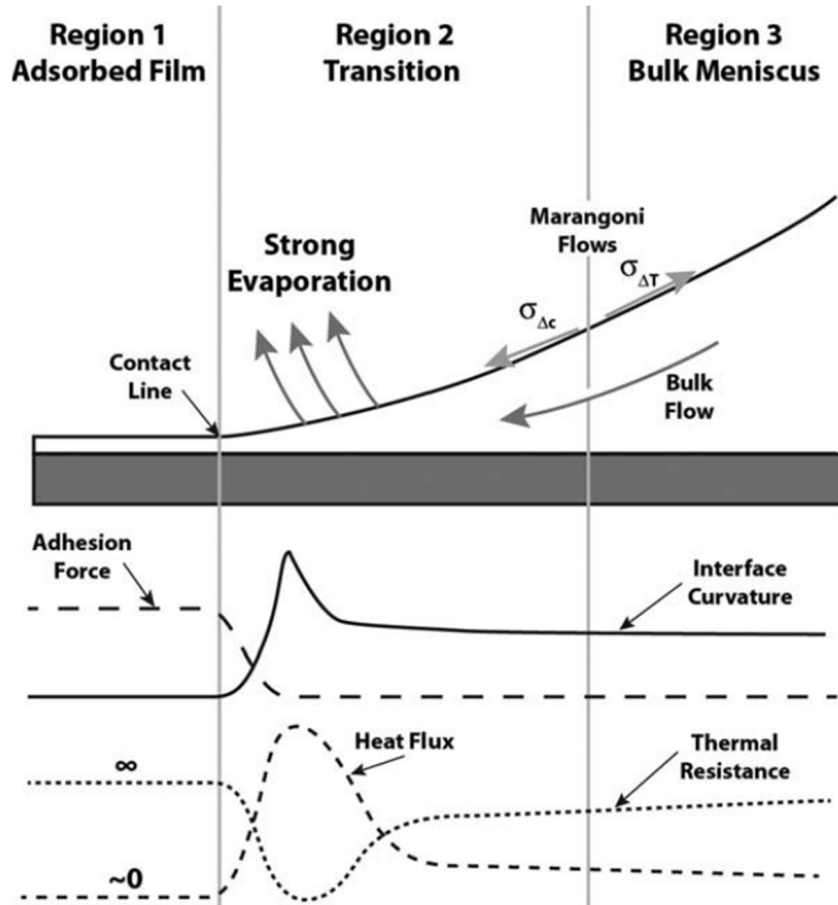


Figure 2-1: Evaporating meniscus regions in thin film evaporation. (Plawsky et al. 2014)

The extended meniscus, or transition region, is used to enhance the thermal transport of the fluid through the wicking surface. This region is the site of thin film evaporation due to its small thickness along with low thermal resistance compared to the bulk meniscus region where larger film thickness and greater thermal resistance exist. To maximize heat dissipation using this heat transfer technique, the evaporative area is to be increased throughout a heated surface. Many studies have been done using a variety of micro/nanostructures configurations and porous wicks as the wicking surfaces creating a larger number of evaporation sites for greater heat removal. Different structure configurations have been explored as Xiao et al. (2010) studied liquid

propagation rates through structured surfaces using cylindrical micropillars along with Ranjan et al (2010) who studied the evaporating meniscus region through packed spheres, vertical and horizontal wires, along with rectangular ribs.

Previous studies have tested the heat dissipation limits for this phase change cooling strategy. Solomon et al. (2016) experimentally characterized fabricated test devices to determine their thermal performance through cylindrical silicon micropillar wicks. Experiments were performed with micropillars having a diameter of $5\mu\text{m}$, height of $82\mu\text{m}$, and $12\mu\text{m}$. Thin film evaporation was observed at a heat flux of 20 W/cm^2 and a dry island that formed furthest from the water reservoir was observed at a heat flux of 46 W/cm^2 where the heat transfer mechanism changed from evaporation to convection, shown in Fig. 2-2.

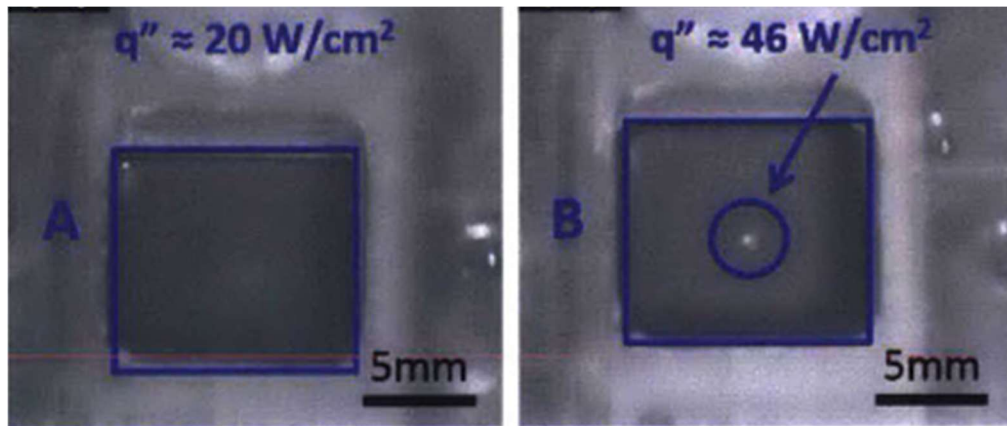


Figure 2-2: High speed images of the test device during steady-state evaporation at $\approx 20\text{ W/cm}^2$ and dry out and thermal run away at $\approx 46\text{ W/cm}^2$ (Solomon et al. 2016)

Determined heat flux was then plotted as a function of the temperature difference between the substrate wall and the chamber for the before mentioned test device, shown in Fig. 2-3. Heat flux was shown to gradually increase as the temperature difference also increased. The two points

are pointed out on the plot where steady state thin film evaporation was observed as well as dry-out detection.

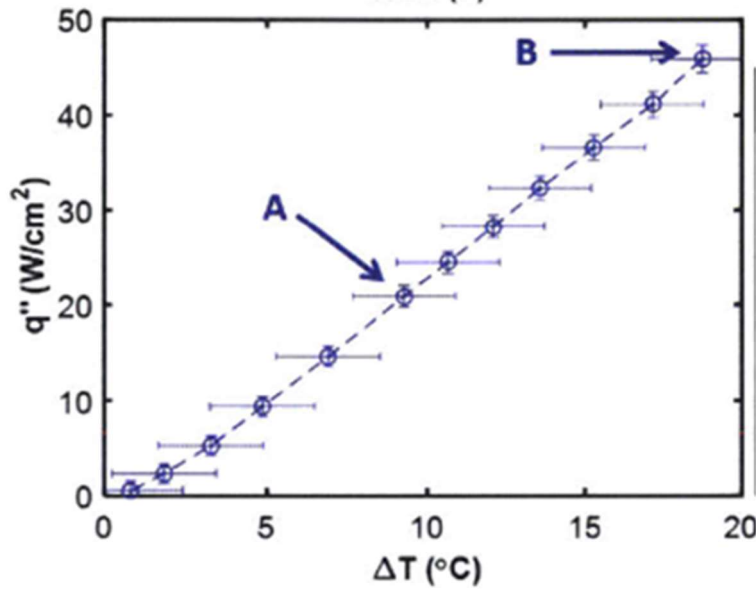


Figure 2-3: Heat flux as a function of temperature difference between the substrate wall and the chamber for device with D, H, and L of 5, 82, and 12 μ m, respectively. (Solomon et al. 2016)

Solomon et al. (2016) also characterized hot spot cooling using thin film evaporation through these silicon micropillars for the same test device. Using thin film evaporation, heat fluxes up to ≈ 6 kW/cm² were dissipated from a 640x620 μ m² footprint area. When viscous losses exceed the capillary pressure a hotspot dry out forms due to insufficient liquid supply. When this dry spot formed, the temperature at this location increased up to $\approx 290^\circ\text{C}$ while neighboring locations remained low at about 50°C. This showed that thin film evaporation is truly useful for dissipation of high heat fluxes while maintaining a low device temperature. A heat flux value of ≈ 6 kW/cm² was dissipated from a single hotspot and shown in Fig. 2-4.

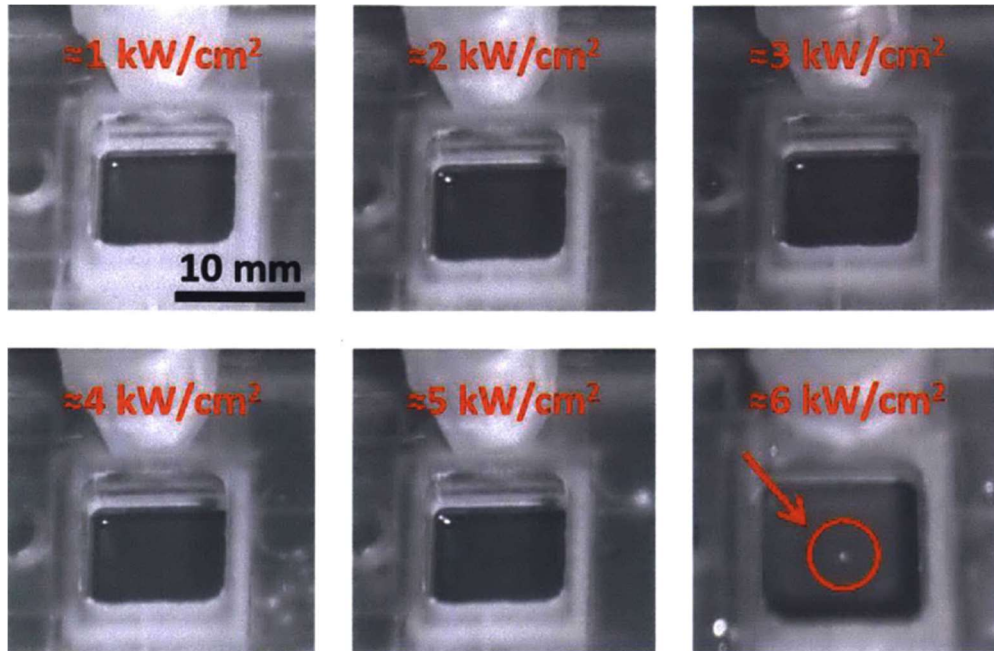


Figure 2-4: Dry out heat flux captured by high-speed camera due to liquid starvation. (Solomon et al. 2016)

To maximize the heat flux through microstructures it is important to understand the effect that the microstructure dimensions have on the amount of heat dissipation. Farokhnia et al. (2016) theoretically and experimentally analyzed the optical dimensions for micro/nanostructures to maximize the interfacial heat flux using thin film evaporation. Different geometries of microstructures were chosen to characterize the optimal configuration for thin film evaporation, shown in Figure 2-5.

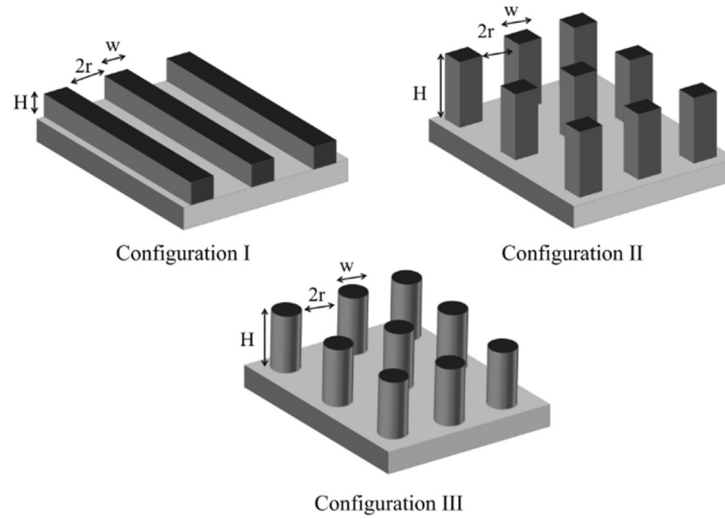


Figure 2-5: Studied model structures for thin-film evaporation: rectangular ribs (configuration I), vertical square pillars (configuration II), and vertical wires (configuration III). (Farokhnia et al. 2016)

Through theoretical modeling, it was determined that the configurations II and III shown an optimal value of width-to-spacing ratio that maximizes the interfacial heat flux for microstructure length of $50\mu\text{m}$ and height of $50\mu\text{m}$. A value of 1.27 and 1.5 were determined for configuration II and III, respectively. Knowing these optimal microstructure dimensions, samples were manufactured using silicon wafers coated with a thin layer of chromium. Samples with various width to spacing ratios with the same density of pillars were developed along with microstructures with the same width to spacing ratio but with varying pillar density. Tests were performed with isopropyl alcohol as the working fluid to increase the wettability of the structures, results between simulations and experimental trails are shown in Figure 2-6 and Figure 2-7.

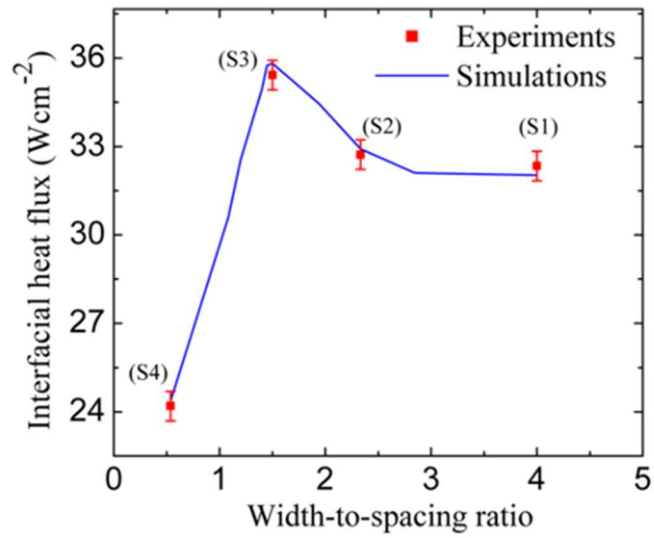


Figure 2-6: Interfacial heat flux values predicted compared to experimental measurements for microstructures with varying width to spacing ratios. (Farokhnia et al. 2016)

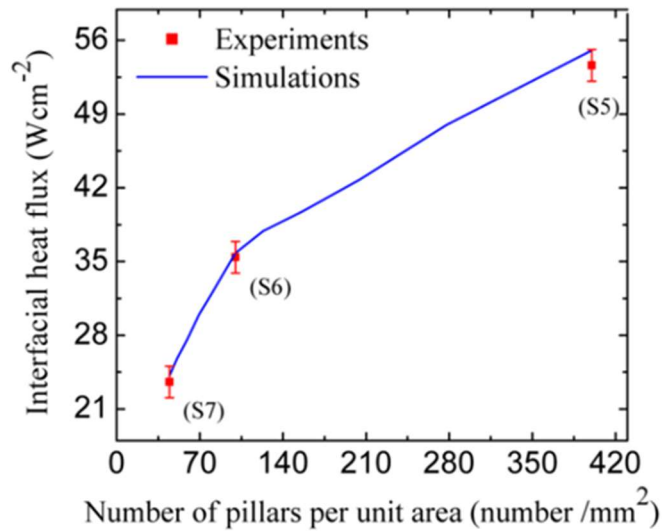


Figure 2-7: Interfacial heat flux values predicted compared to experimental measurements for microstructures with same width to spacing ratios but varying density of pillars. (Farokhnia et al. 2016)

Plawsky et al. (2014) suggest that altering the surface chemistry and surface topography of the microstructures can lead to enhanced vaporization from these surfaces. Tailoring the substrate properties along with the liquid to solid interactions have seen significant advancements in effective heat removal. To efficiently understand these liquid and solid interactions it is important to know how the working fluid responds to the selected substrate material. Surface wettability plays an important factor in how well the working fluid can wick through manufactured microstructures. Hydrophilic surfaces maximize the contact area with the fluid through attractive forces such as molecular bonding, dipole interactions, and Van der Waals forces that attract or repulse atoms. On the other hand, hydrophobic surface minimizes contact area with the fluid through repulsive forces. These different types of surfaces affect the contact angle between the working fluid and the substrate surface. Studies done by Orlova et al. (2015) show contact angles of water on copper substrates with different roughness ranging from 60-87°. It was determined that increasing surface roughness led to an increase in contact angle. Ranjan et al. (2011) developed a numerical model for the evaporating liquid meniscus in wick structures using the solid-liquid combination of copper-water and considered various contact angles to determine the effects on evaporation. Results show that with increasing contact angle there is a decrease in the substrates heat flux as a function of meniscus height, shown in Fig. 2-8.

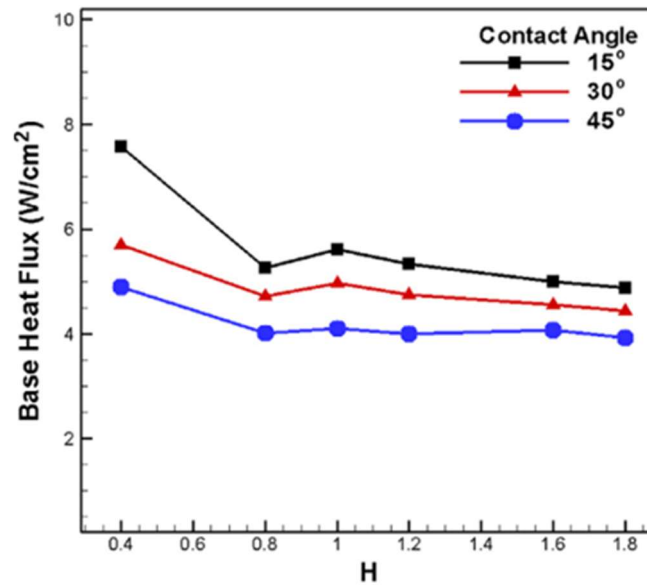


Figure 2-8: Variation of base heat flux with meniscus level for various contact angles. (Ranjan et al. 2016)

Another key factor that affects heat transfer performance through thin film evaporation is capillary pressure. This difference in pressure throughout a wicking surface determines the rate of suction of a fluid through these microstructures. Models by Ranjan et al. (2009) studied wicking characteristics through four well-defined microstructures for various contact angles. Values of capillary pressure were determined for decreasing pore sizes between the microstructures, showing optimal values for suction, or wicking, of the fluid through these microstructures. Effects of porosity on capillary pressure were presented and showed that higher porosity leads to a decrease in maximum possible capillary pressure.

Based on existing literature, it is key to understand the liquid-solid interactions and microstructure optimization to be able to maximize heat dissipation for a manufactured surface. Thin film evaporation is a proven efficient two-phase heat transfer solution with multiple theoretical models established to predict its cooling capabilities. Optimal microstructure

dimensions and fluid properties are vital in increasing the surface heat flux leading to highly efficient cooling solutions. This motivated this work in designing a setup that uses this phase change cooling solution to experimentally characterize the heat transfer capabilities of manufactured surfaces with micropillar arrays using rectangular microstructures with known dimensions.

2.2 Heat Pipe Thermal Management

Based on previous studies done experimentally and values obtained from simulations, heat dissipation rates achieved by thin film evaporation make this cooling strategy ideal to be incorporated in high heat flux environments. The working principle of thin film evaporation has been incorporated into heat pipe, a fully sealed passive two-phase heat transfer device that takes advantage of a fluids high latent heat of vaporization, leading to efficient heat transfer, shown in Fig. 2-9. This capillary-based heat transfer device was first demonstrated in the 1960's (Shukla 2015) and later, was first used for the thermal equilibration of satellite transponders. Since then, heat pipes have been incorporated in spacecraft cooling, electronic components in satellites, and computers.

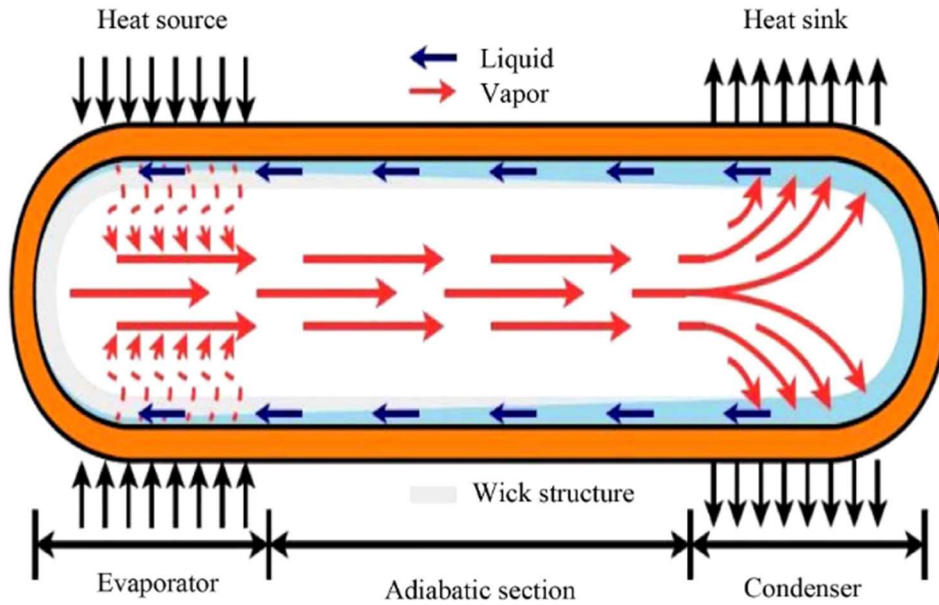


Figure 2-9: Schematic of a heat pipe. (Shukla 2015)

The working fluid of the heat pipe is processed under vacuum conditions, allowing for two-phase heat transfer across a wide temperature range along the device. A heat pipe is made up of three sections: an evaporator, wick, and condenser section. Heat is inputted into the evaporator section causing the working fluid to boil, leading to isothermal expansion. The vapor then travels to the condenser section, the low pressure/colder section of the heat pipe, through an adiabatic section. It is at this point where the vapor gives up its latent heat and condenses back into a liquid, or isothermal compression, and is absorbed by the microstructures/wicking structures that passively pump the fluid back into the evaporator. This is aided by the capillary pressure created by the menisci along the wicking surface such as axial grooves, mesh screen, sintered metal powder grooves and micro/nanostructures. This cooling technique is most prominent due to its high reliability, small size, lightweight, and zero needed maintenance. Working fluids for heat pipes range from helium and nitrogen for cryogenic applications to liquid metals including mercury, sodium, and indium for high temperature environments.

A copper heat pipe with water as the working fluid is most used for the cooling of electronics. Due to water's high latent heat of vaporization it makes it a very popular working fluid due to its high figure of merit. The merit number is based on the fluid properties, and this determines the maximum power the heat pipe can withstand when it is capillary limited. A model showed by Chaudhry et al. (2012) shows the figure of merit for various fluids across a 100K temperature range, shown in Fig. 2-10. It is seen that water is the best working fluid candidate and has been historically used in heat pipes for efficient thermal management.

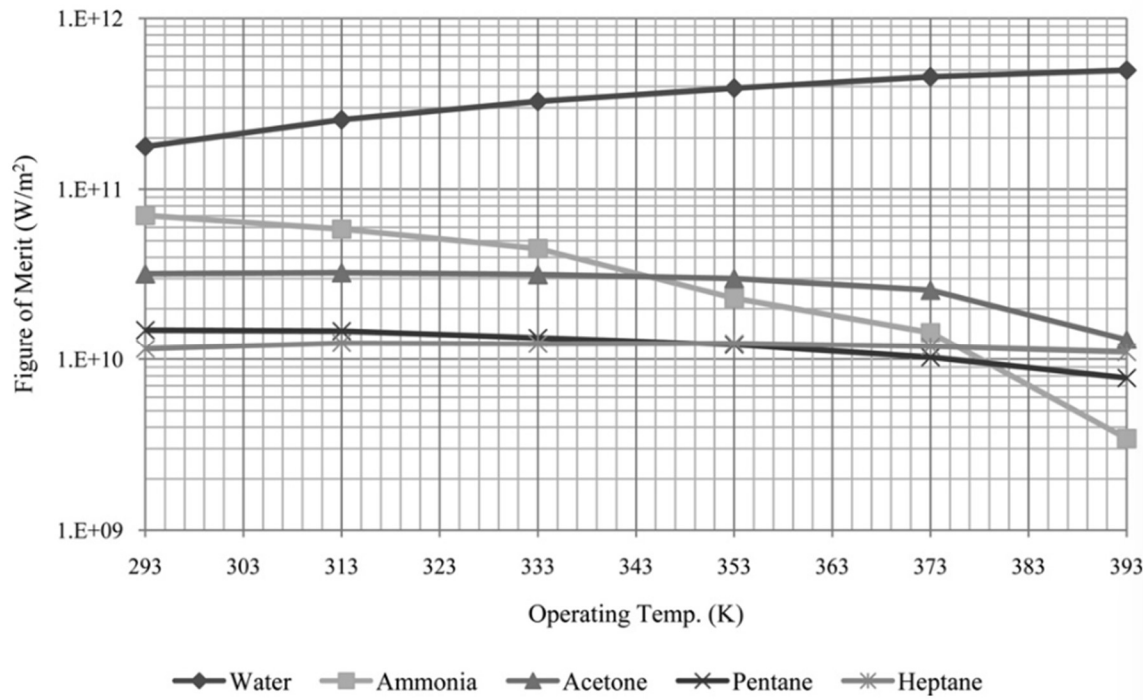


Figure 2-10: Figure of merit for various heat pipe working fluids. (Chaudhry et al. 2012)

Aside from having the best figure of merit compared to other popular working fluids, water also presents great wicking power. Anderson et al. (2008) discussed a cooling design using a copper-water heat pipe to cool concentrating photovoltaic systems by natural convection. A copper-water heat pipe was selected due to compatibility and far superior wicking capabilities of

water on the copper surface, shown in Fig 2-11. The proposed heat pipe was able to dissipate 40 W/cm² to the environment with a total cell-to-ambient temperature of only 40°C while cooling with a single copper block would have a temperature difference of up to 210°C.

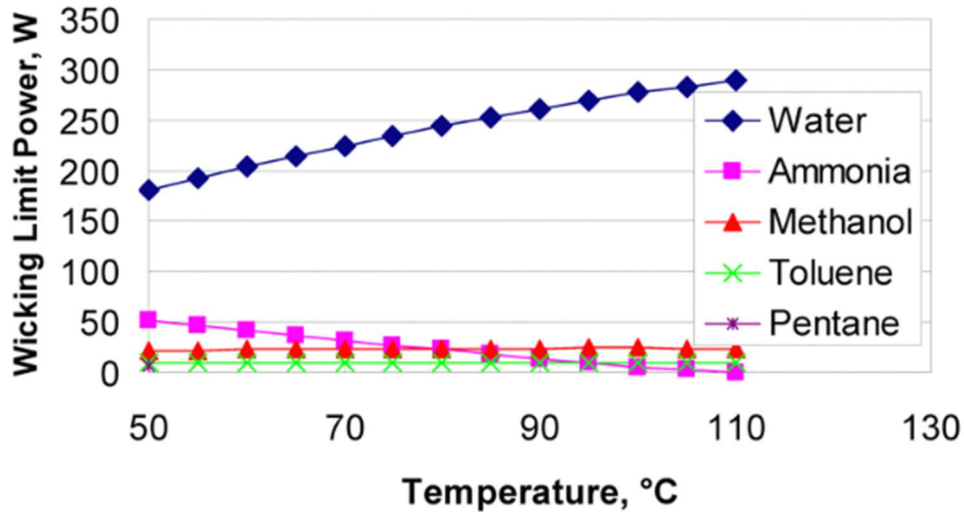


Figure 2-11: Heat pipe wicking limit for various working fluids of proposed wicking surface. (Anderson et al. 2008)

The effect of capillary pressure was studied by Wang et al. (2005) who developed a novel flat heat pipe for the thermal management in high power microelectronics, power converting systems, laptop computers and spacecraft control systems with sintered copper screen mesh used as the wicking surface with a series of parallel wires allowing for the flow of the fluid. Two prototypes were created with different number of layers of mesh screen providing variable wicking surfaces and results showed that the device with the greater amount of screen layers was able to dissipate 19.1 W/cm² while the other dissipated 17.4 W/cm². Theoretical models displayed the effect of the wicking surface thickness on the maximum heat transport for a proposed heat pipe. Models showed that the more porous a wicking surface is, the greater the amount of heat dissipation.

The ability of a heat pipe to dissipate heat from a concentrated heat load makes these heat transfer devices reliable and a vital tool for thermal management. Many studies have been done with a copper-water proposed heat pipes for the thermal management of electronics. Hayat et al. (2020) studied copper foam-based heat sinks for the thermal management of electronic systems with water as the working fluid. The test substrates were subjected to various heat fluxes ranging from 2-3 kW/m² and results showed that after 100 minutes there was 50% temperature reduction. Ivanova et al. (2006) explored the feasibility of a cooling system with miniature copper heat pipes for embedded electronics with water as the working fluid. The heat transfer limits of these heat pipes were explored and determined that each had the capacity to transfer more than 110W without experiencing dry out at the evaporator. Li et al. (2016) investigated the thermal performance of a copper-water flat heat pipe with a novel wicking surface having diameters ranging from 50-100 μ m and a 1mm thin liquid film. The proposed heat pipe was able to effectively dissipate 100 W/cm² with very small thermal resistance. Temperature readings comparing the heat pipe with a copper sheet at an applied heat load were compared. The heat pipe showed a much more even temperature distribution with $\approx 3^{\circ}\text{C}$ difference throughout the body compared to $\approx 8^{\circ}\text{C}$ difference of a copper sheet.

The characterization of the manufactured samples in this work will lead to an understanding of the evaporator section of a fully engineered heat pipe. Obtained heat fluxes will be compared for samples having varying microstructure dimensions for optimization of heat transfer capabilities. Based on available literature, a heat pipe is the most promising cooling solution for thermal management at high heat fluxes and has been implemented along various applications and areas of study. Being able to remove heat from a concentrated heat load allows for better thermal managements for aerospace, deep space, electronics, and defense applications.

Chapter 3: Theoretical Approach

3.1 Theoretical Approach

A theoretical model to plot the expected capillary limited dry-out heat flux was adapted from previous thin film evaporation studies done by Solomon (2016) to plot the expected dry-out heat flux against wall-to-wall spacing between micropillars. This model considers both material and fluid properties for the selected liquid-solid combination. Multiple test samples with various micropillar heights were manufactured and were tested to determine the effect on the dry-out heat flux.

The ability of the test sample to transmit fluid, known as permeability, was determined. Micropillar dimensions a , b , h are the diameter, wall-to-wall spacing, and height of the micropillars, respectively. 2D permeability relation was used from Sangani et al. (1982) and Xiao et al. (2011) for this theoretical model. Micropillar spacing and diameter was used to determine the two-dimensional permeability, not accounting for micropillar height. Using Eq. 1 and Eq. 2, the 2D permeability relation was calculated using Eq. 3.

$$c = \frac{\pi d^2}{4b^2} \quad (1)$$

$$z = \ln(c^{0.5}) - 0.738 + c - 0.887c^2 + 2.038c^3 \quad (2)$$

$$K_{2D} = (b^2) \left(\frac{z}{4\pi} \right) \quad (3)$$

Porosity, the measure of the void spaces on the test sample surface, was then determined. Porosity of the $1 \times 1 \text{ cm}^2$ micropillar wick section was calculated using Eq. 4. Micropillar dimensions varied for each manufactured sample that was tested.

$$\varepsilon = 1 - \frac{\pi d^2}{4b^2} \quad (4)$$

A geometric parameter was used to express a relationship between the porosity and the two-dimensional permeability of each of the samples. This geometric parameter, β , was calculated using Eq. 5.

$$\beta = \sqrt{\frac{\varepsilon}{K_{2D}}} \quad (5)$$

The capillary pressure of the wick section is known as the force due to the pressure difference between the vapor and liquid side of the meniscus, as stated by Solomon et al. (2016). This pressure is the driving force of the fluid through the wicking surface and was calculated using Eq. 6 where θ is the contact angle of water on the targeted test sample material. A contact angle of 87° its take for water on a copper surface (Orlova et al. 2015)

$$P_c = \frac{4\sigma_{LV} \cos(\theta)}{d \left(\frac{4}{\pi} \left(\frac{b}{d} \right)^2 - 1 \right)} \quad (6)$$

The actual micropillar height, h^* , is calculated knowing the effect of the meniscus and its relationship with the receding contact angle. The actual micropillar height was calculated using Eq. 7.

$$h^* = h - \frac{(\sqrt{2}b - d)(1 - \sin(\theta))}{2 \cos(\theta)} \quad (7)$$

The effective micropillar height is determined by assuming a linear relation in its height from the edge of the micropillar to the center and was determined using Eq. 8.

$$h_{eff} = \frac{1}{2}(h + h^*) \quad (8)$$

Knowing the parameters stated above, the effective permeability is then calculated using several correction factors ($\xi, \Lambda_1, \Lambda_2$) shown in Eq. 9, 10 and 11. The effective permeability was then calculated using Eq. 12.

$$\xi = \frac{\varepsilon d}{4(1 - \varepsilon)} \quad (9)$$

$$\Lambda_1 = \frac{h_{eff}}{h} \quad (10)$$

$$\Lambda_2 = \frac{h_{eff} + \xi}{h + \xi} \quad (11)$$

$$K_{eff} = K_{2D} \left(1 - \frac{e^{2\beta h_{eff}} - 1}{\beta h_{eff} (e^{2\beta h_{eff}} + 1)} \right) \Lambda_1 \Lambda_2 \quad (12)$$

Calculating the theoretical dry-out heat flux is now possible by knowing the effective parameters of the sample. A figure of merit is expressed for the selected surface/working fluid and was calculated using Eq. 13

$$M = \frac{\sigma_{LV} \rho_l h_{fg}}{\mu_l} \quad (13)$$

where ρ_l is the liquid density, h_{fg} is the liquid to vapor latent heat of evaporation, and μ_l is the dynamic viscosity of the fluid. This expression considers all fluid properties which determine the heat carrying capacity of the fluid. Fluid properties used for this model are shown in Table 3-1.

Table 3-1: Fluid properties of water used for calculations.

Fluid Property	Unit
Contact Angle of Water on Copper	87°

Liquid to Vapor Surface Tension of Water	$0.0763 \frac{N}{m}$
Liquid Density of Water	$997 \frac{kg}{m^3}$
Liquid to Vapor Latent Heat of Evaporation of Water	$2442000 \frac{J}{kg}$
Dynamic Viscosity of Water	$0.000891 \frac{kg}{m*s}$

An effective geometric parameter is calculated, using the relation in Eq. 6, considering the calculated effective permeability of the sample, and was calculated using Eq. 14.

$$\beta_{eff} = \sqrt{\frac{\varepsilon}{K_{eff}}} \quad (14)$$

This parameter was then used to determine a dimensionless parameter, ψ , which relates the porosity and effective permeability that are calculated from the micropillar geometries. This parameter is expressed and calculated using Eq. 15.

$$\psi = \frac{h_{eff}K_{eff} \left(1 - \frac{\tanh(h_{eff}\beta_{eff})}{h_{eff}\beta_{eff}} \right)}{l^2 d \left(\left(\frac{4}{\pi} \right) \left(\frac{b}{d} \right)^2 - 1 \right)} \quad (15)$$

The capillary limited dry-out heat flux is then calculated using the effective parameters, the fluid heat carrying capacity, and the fluids receding contact angle, shown in Eq. 16.

$$q'' = \left(\frac{40}{3} \right) \psi M \cos\theta \quad (16)$$

Based on this theoretical model, a plot was made for the manufactured test samples with different micropillar dimensions using Eq. 1-16.

Chapter 4: Experimental Setup

4.1 Test Facility

An experimental setup was designed and assembled to determine each samples thermal management capabilities based on previous studies done by Solomon et al. (2016). The objective of these experiments was to find the capillary limited dry-out heat flux of each of the manufactured sample with known micropillar dimensions. The thin film evaporation test facility schematic and piping and instrumentation diagram are shown in Fig. 4-1 and Fig. 4-2.

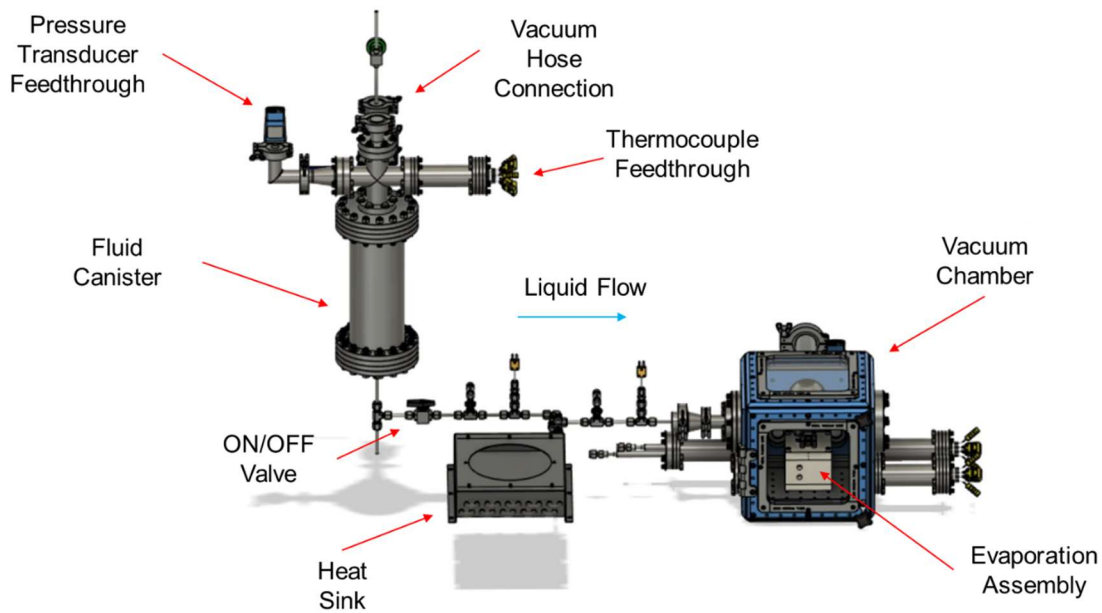


Figure 4-1: CAD of water thin film evaporation test facility.

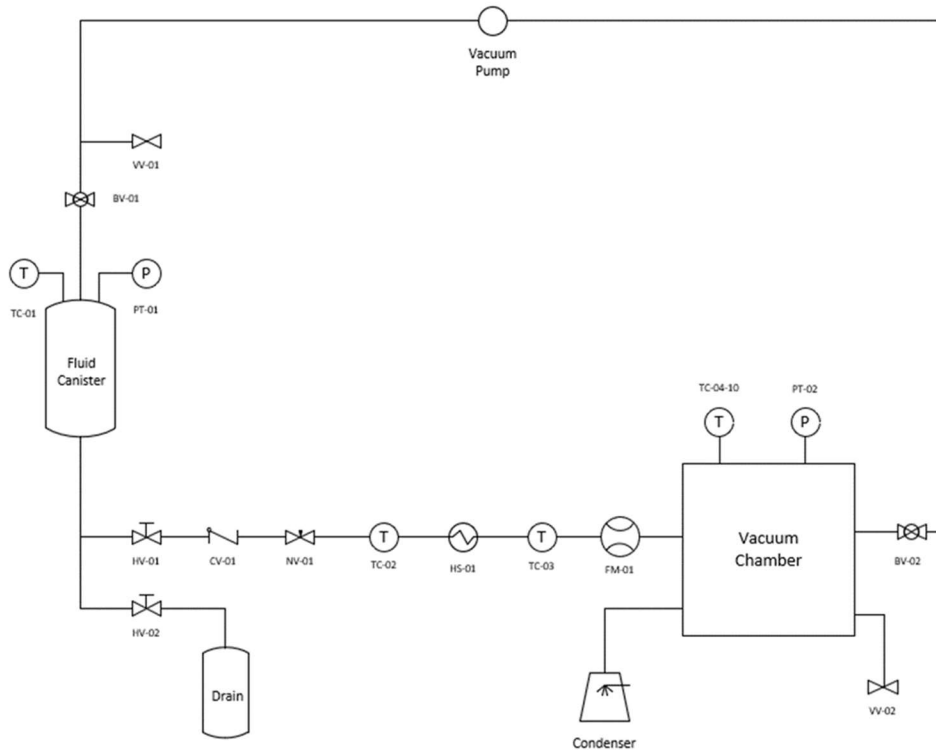


Figure 4-2: P&ID of thin film evaporation facility.

The experimental setup was divided into four main sections that together make up the entire assembly. The setup consists of the evaporation assembly, vacuum chamber, fluid canister, and the main tubing line that supplies the fluid to the sample, the assembled test facility if shown in Fig. 4-3. The fluid canister serves as the liquid container and pressure build up site as liquid is heated up. The fluid is solely pressure driven by the pressure differential between the fluid canister and the vacuum chamber. The heat sink located along the tubing line allows for cooling of the fluid to the targeted temperature of 24° as it enters the vacuum chamber and onto the test surfaces. The evaporation assembly consists of instrumentation that allow for heating control and data acquisition throughout thin film evaporation tests for determining the dry-out heat flux.

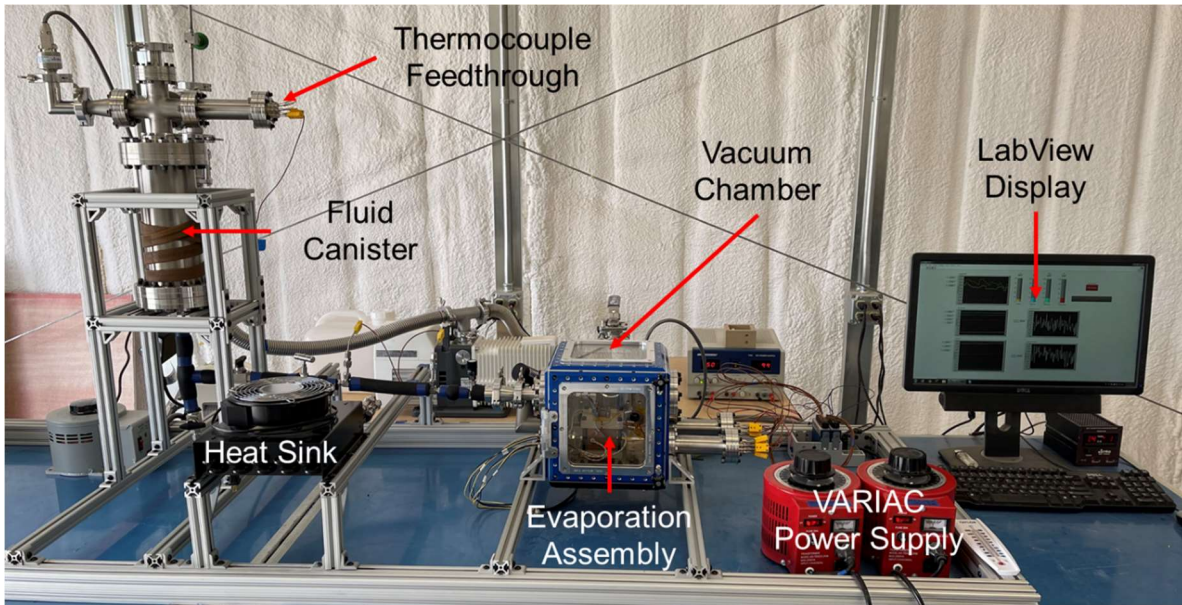


Figure 4-3: UTEP thin film evaporation test facility.

4.1.1 Chamber

A modular vacuum chamber was selected for the vacuum chamber of this experimental setup. A 9" 6061-T6 aluminum alloy cube vacuum chamber frame (Ideal Vacuum) was used to attach three multiport 9x9" chamber plates (Ideal Vacuum), two 9x9" tempered glass viewing window plates (Ideal Vacuum), and one 9x9" heater plate (Ideal Vacuum). Each multiport chamber plate consisted of two CF 2.75 flanges and one CF 4.5 flanges. A CF 2.75 electrical feedthrough is attached to one of the multiport chamber plates and is used to connect the cartridge heater terminals from the interior and connected externally to their corresponding pins connected to a VARIAC power supply. A liquid feedthrough with all necessary adapters is connected to the CF 4.5 flange to allow for liquid supply into the chamber and into the sample assembly. Two 5 pair type K thermocouple feedthroughs are connected to the second multiport chamber plate that allows for temperature readings inside the vacuum chamber. The third multiport chamber plate located on the back of the vacuum chamber includes all pressure management and monitoring components.

These components include a Micro Pirani Series 925 pressure transducer, vent valve, and the vacuum line that connects to the setups vacuum pump (Kinney Tuthill KVAC-21 KVAC21 Pascal Dual Stage Rotary Vane Vacuum Pump). The fully assembled modular vacuum chamber is shown in Fig. 4-4 and Fig. 4-5.

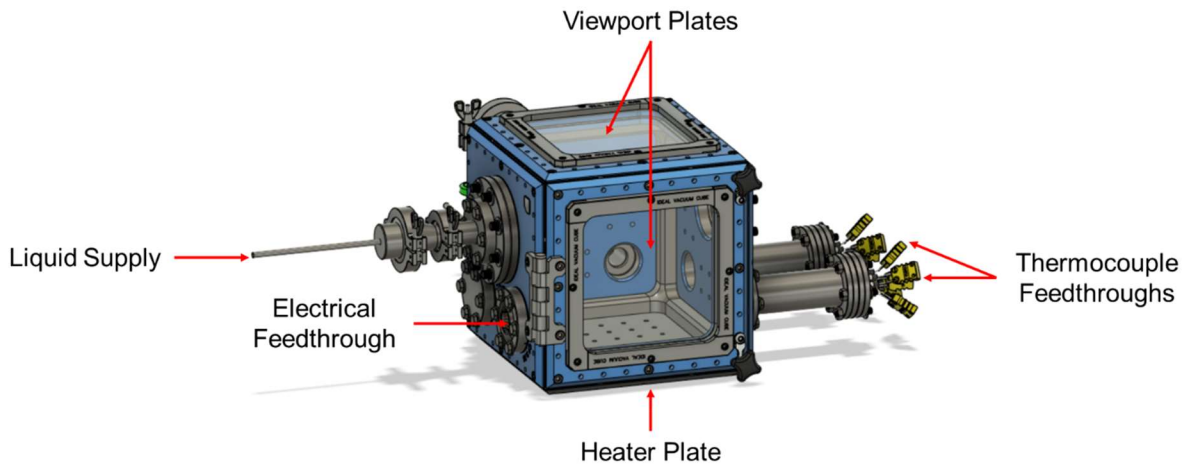


Figure 4-4: Front view of the modular vacuum chamber with attached feedthroughs and flanges.

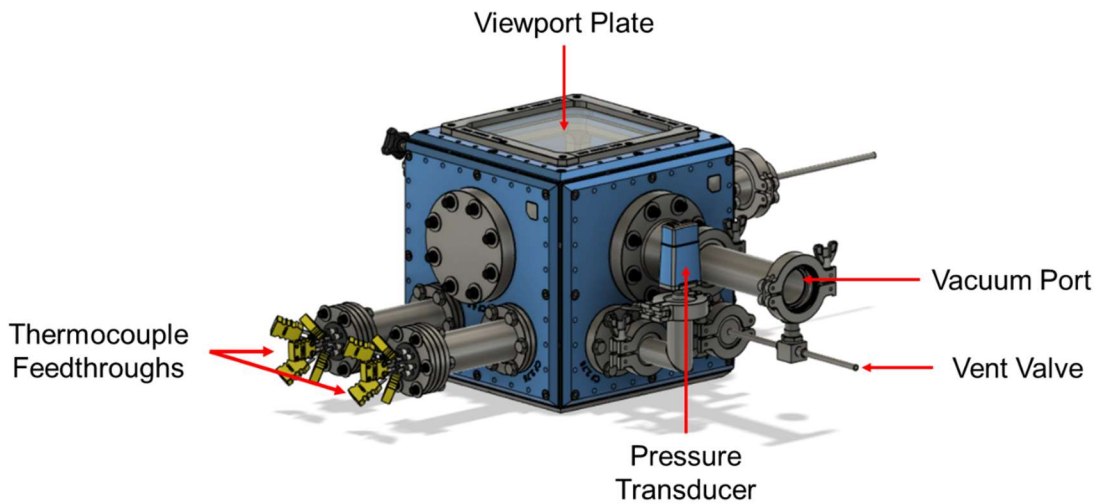


Figure 4-5: Back view of the modular vacuum chamber with attached feedthroughs and flanges.

The thin film evaporation assembly was then connected to the liquid supply feedthrough from the inside of the chamber. The 6.35 mm Swagelok elbow on the test sample is connected to

the corresponding Swagelok terminals of the liquid supply line. The assembly is placed inside ensuring it is structurally supported, and cartridge heater terminals are connected to the corresponding pins on the electrical feedthrough located on the left wall of the chamber. A sliced view of the evaporation assembly inside the vacuum chamber is shown in Fig. 4-6.

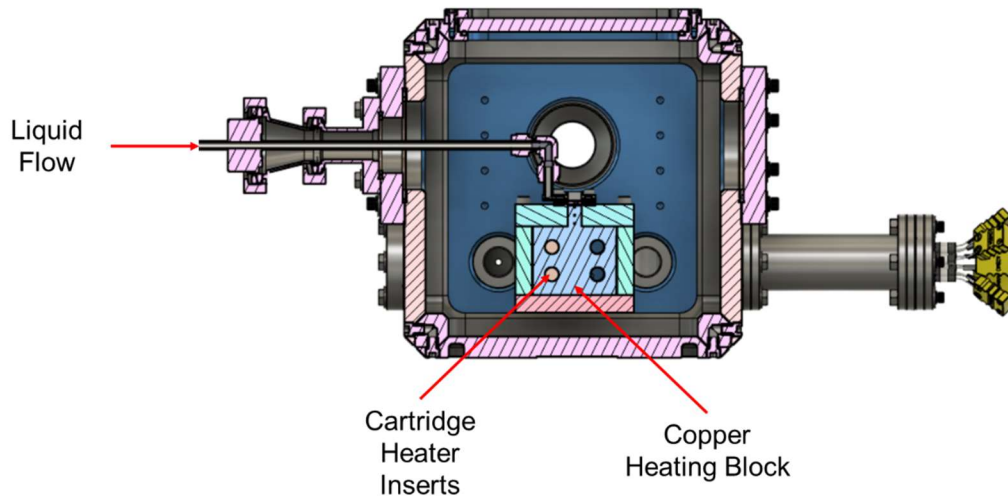


Figure 4-6: Sliced view of evaporation assembly connected inside vacuum chamber.

4.1.2 Fluid Canister

The fluid canister was made up of a CF 6 stainless steel full nipple with reducers to CF 2.75 on each end. The top end of the canister included a CF 2.75 5-way cross that allowed for all necessary feedthroughs for temperature and pressure readings, vacuum line for pressure management, and access port for filling up the canister with the working fluid. One Type K thermocouple was placed on the inside of the canister to allow for the temperature readings of the bulk fluid. A Micro Pirani Series 925 pressure transducer is used for pressure readings inside the canister, all readings are displayed on LabVIEW. At the bottom flange of the canister a CF 2.75 to 6.35 mm Swagelok adapter is attached to connect the canister assembly to the tubing lines. A

rope heater with adjustable temperature control is wrapped around the canister from the outside to heat up the fluid. The assembled fluid canister is shown in Fig. 4-7.

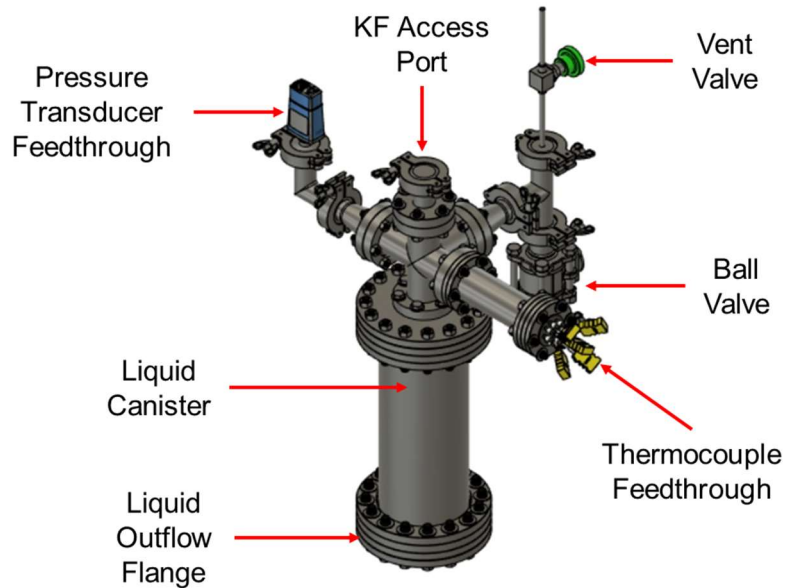


Figure 4-7: Fluid canister with attached flanges and feedthroughs.

As the fluid is being heated, pressure in the canister increases. Manual hand valves are used to close or open the flow from the canister into the main tubing line. Initially, these valves are closed to allow for pressure build up inside the canister assembly. Once ready, the hand valve on the main tubing lines opened to allow for the flow of this heater water. Along the tubing, a heat sink for water (McMaster-Carr) was installed and connected to a VARIAC power supply to adjust its cooling capability based on fluid temperature and vacuum pressure conditions. Thermocouples are located before the fluid enters the heat sink and right before the flow adjusting valve to monitor temperature and how much the fluid is being cooled. A low flow metering valve is located before the fluid enters the vacuum chamber to control and adjust the flow rate.

4.1.3 Test Surfaces

A conventionally manufactured flat sample was designed and manufactured out of copper. These samples consisted of two parts, the primary reservoir with a $1 \times 1 \text{ cm}^2$ micropillar array (Fig. 4-8a) and the secondary reservoir with a 6.35 mm diameter tube (Fig. 4-8b) in which a 6.35 mm Swagelok elbow connects to the liquid supply line inside the vacuum chamber. Multiple samples were manufactured to test and determine the effect the material of sample has on the capillary dry-out heat flux. A liquid gasket is made from Permatex High Temperature Gasket Maker and placed between the two parts to seal and avoid any leaks throughout the test.

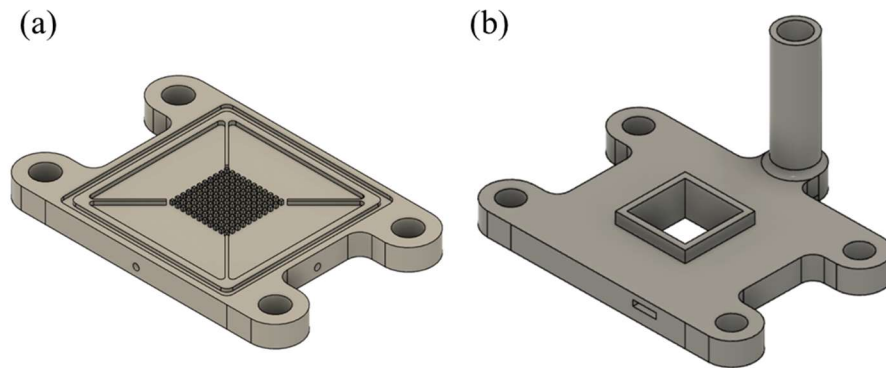


Figure 4-8: (a) Primary reservoir with micropillar array. (b) Secondary reservoir.

As the working fluid enters the test sample, it is introduced through the attached 6.35 mm Swagelok elbow and into the secondary reservoir. The secondary reservoir incorporates four circular slots for water to drip down into the primary reservoir, shown in Fig. 4-9. A drain excess port on the secondary reservoir was included to dispatch any excess water entering the sample assembly once both the primary and secondary reservoirs are filled.

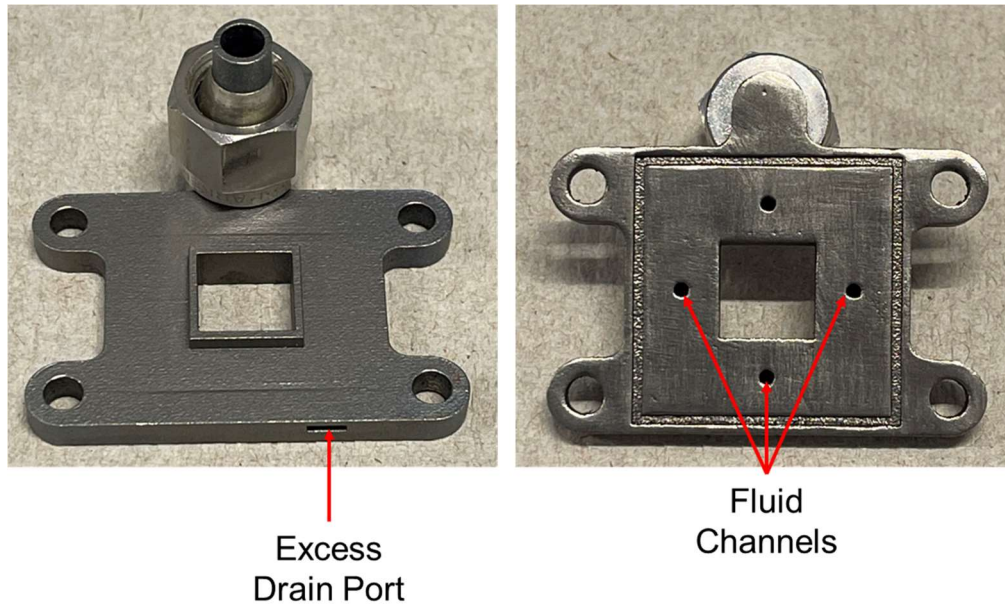


Figure 4-9: (a) Top view of primary reservoir. (b) Bottom view primary reservoir.

Water is then introduced into the four primary reservoirs and once filled, onto the micropillar array by capillary wicking. Test samples were designed in a way that the primary reservoirs remain filled throughout the test. A sliced view of both the primary and secondary reservoirs are shown in Fig. 4-10.

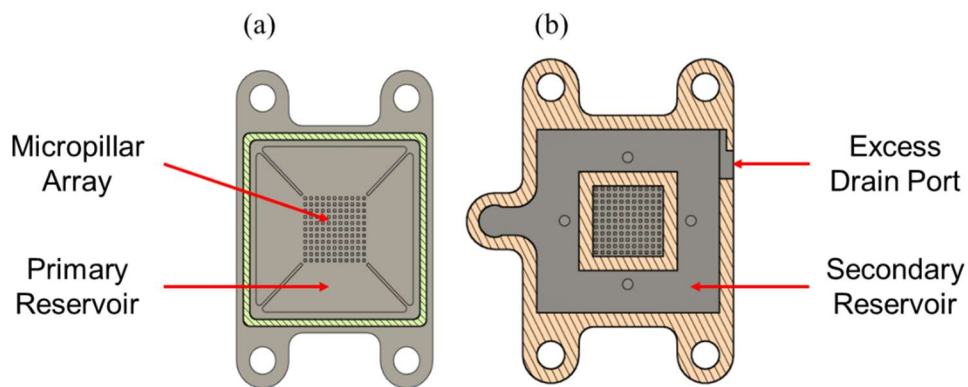


Figure 4-10: (a) Sliced view of primary reservoir. (b) Sliced view of secondary reservoir.

Conventionally manufactured test samples made of copper were tested. Samples were designed with micropillar hydraulic diameter of 400 μm , various micropillar spacings ranging from 500-1100 μm , and heights of 500 and 600 μm were tested to determine the effect on the capillary limited dry-out heat flux. Manufactured test sample with labeled components is shown in Fig. 4-11 along with all the manufactured test samples presented in Table 4-1.

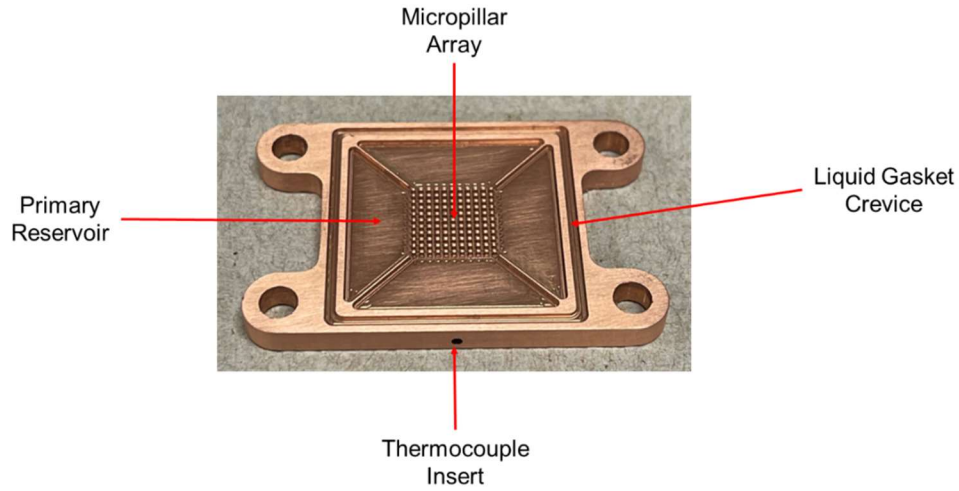


Figure 4-11: Labeled manufactured test sample.

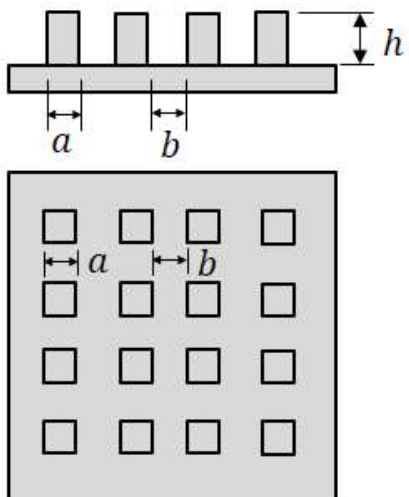


Figure 4-12: Labeled micropillar array schematic with micropillar diameter, spacing, and height (a, b, and h).

Table 4-1: Manufactured test sample micropillar dimensions.

Test Sample	Diameter (μm)	Spacing (μm)	Height (μm)
1	400	500	500
2	400	500	600
3	400	800	500
4	400	1100	500

SEM images were obtained and shown in Fig. 4-13 through Fig. 4-16 for all manufactured samples to determine the actual micropillar dimensions. These dimensions were accounted for and were used to develop the true theoretical prediction to compared to the obtained experimental results.

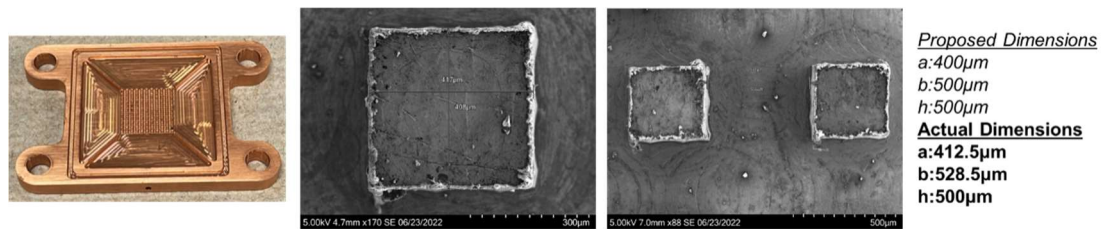


Figure 4-13: SEM images and averaged dimensions for manufacture sample having micropillar dimensions a=400 μm b=500 μm and h=500 μm .

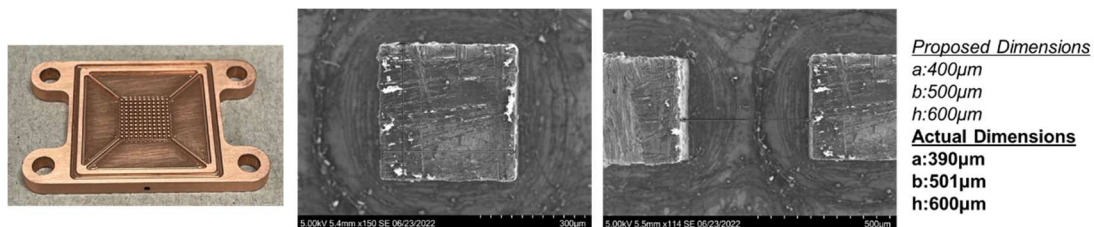


Figure 4-14: SEM images and averaged dimensions for manufacture sample having micropillar dimensions a=400 μm b=500 μm and h=600 μm .

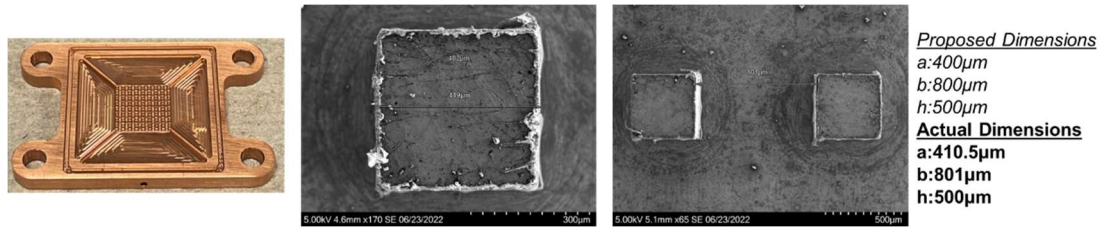


Figure 4-15: SEM images and averaged dimensions for manufacture sample having micropillar dimensions $a=400\mu\text{m}$ $b=800\mu\text{m}$ and $h=500\mu\text{m}$.

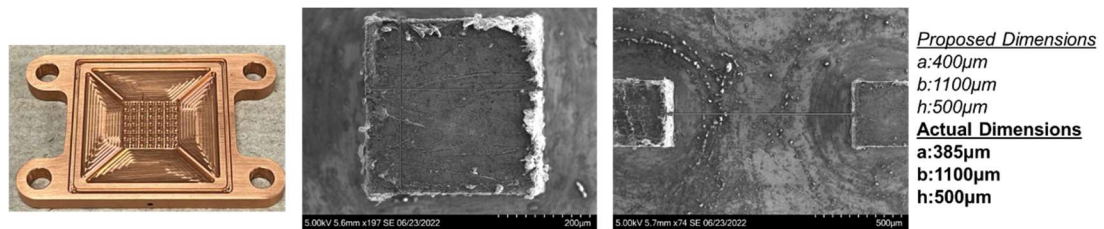


Figure 4-16: SEM images and averaged dimensions for manufacture sample having micropillar dimensions $a=400\mu\text{m}$ $b=1100\mu\text{m}$ and $h=500\mu\text{m}$.

4.1.4 Heater Block

The copper heating block is insulated to reduce convective heat losses. The insulator block made of the insulating material PEEK is divided into three sections which hug the copper block to insulate and reduce any thermal losses from heat being supplied and conducted onto the sample. The assembly is secured and compressed using four 1/4"-20 screws. The evaporation assembly schematic is shown in Fig. 4-17, and a sliced view is shown in Fig. 4-18.

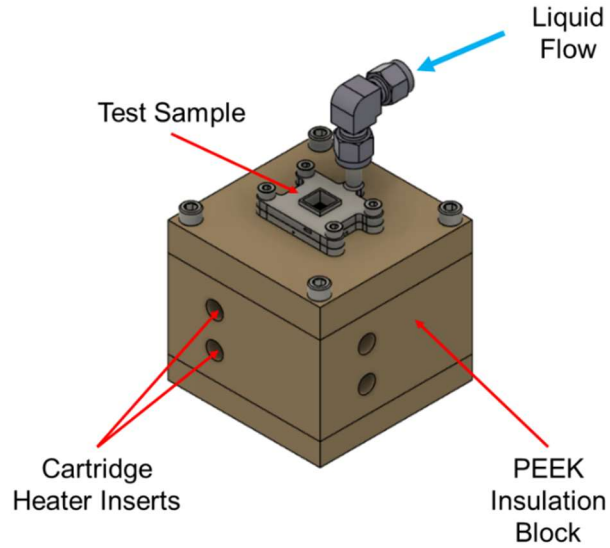


Figure 4-17: Thin film evaporation assembly with attached test sample.

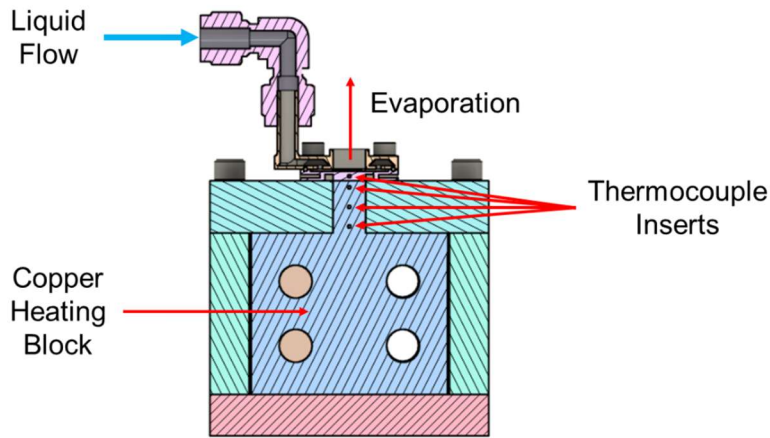


Figure 4-18: Sliced view of the evaporation assembly with attached sample.

Once assembled, the test sample is then placed and secured on the evaporation assembly. This assembly consists of a copper heating block, an additively manufactured insulation block, and eight cartridge heaters. The copper heating block, shown in Fig. 4-19, was manufactured with eight circular slots in which the 9.525 mm wide, 31.75 mm long cartridge heaters are inserted for heating. The copper block neck has three 1 mm diameter slots, 6 mm apart, for the insertion of

fine tip thermocouples for temperature readings leading up to the heated flat sample. The fully assembled evaporation assembly connected interiorly is shown in Fig. 4-20.

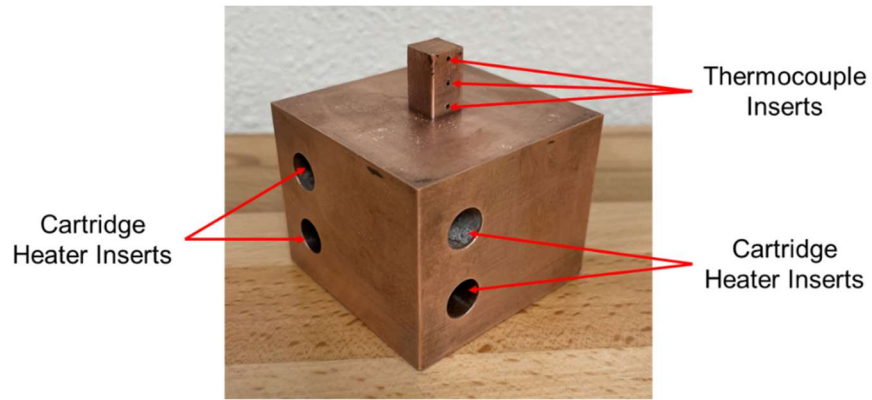


Figure 4-19: Manufactured copper heating block.

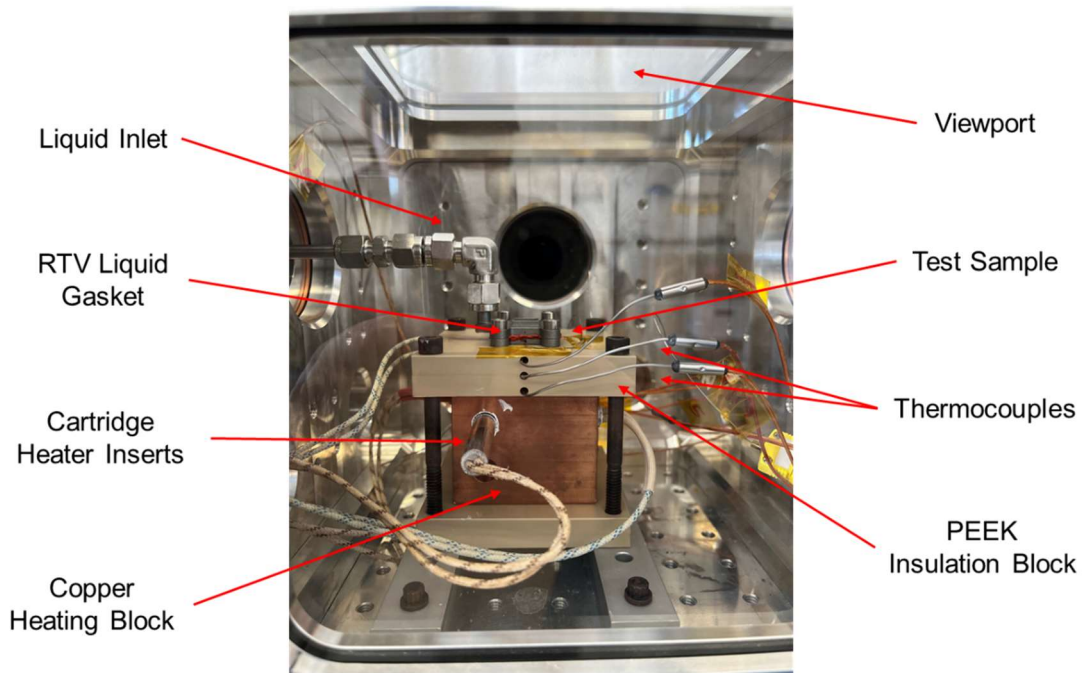


Figure 4-20: Interior components of the vacuum chamber assembled and connected.

4.1.5 Data Acquisition System & LabVIEW

All temperature and pressure readings are displayed and monitored using the test facility LabVIEW display. An NI-9214 module was used to connect all the setup thermocouples along the fluid canister, tubing line and vacuum chamber to the display. Data was collected at 4 samples per second. The canister and chamber pressure transducers were connected to an NI-9205 module and a DC power supply was used to power on these sensors. The test facility LabVIEW display is shown in Fig. 4-21.

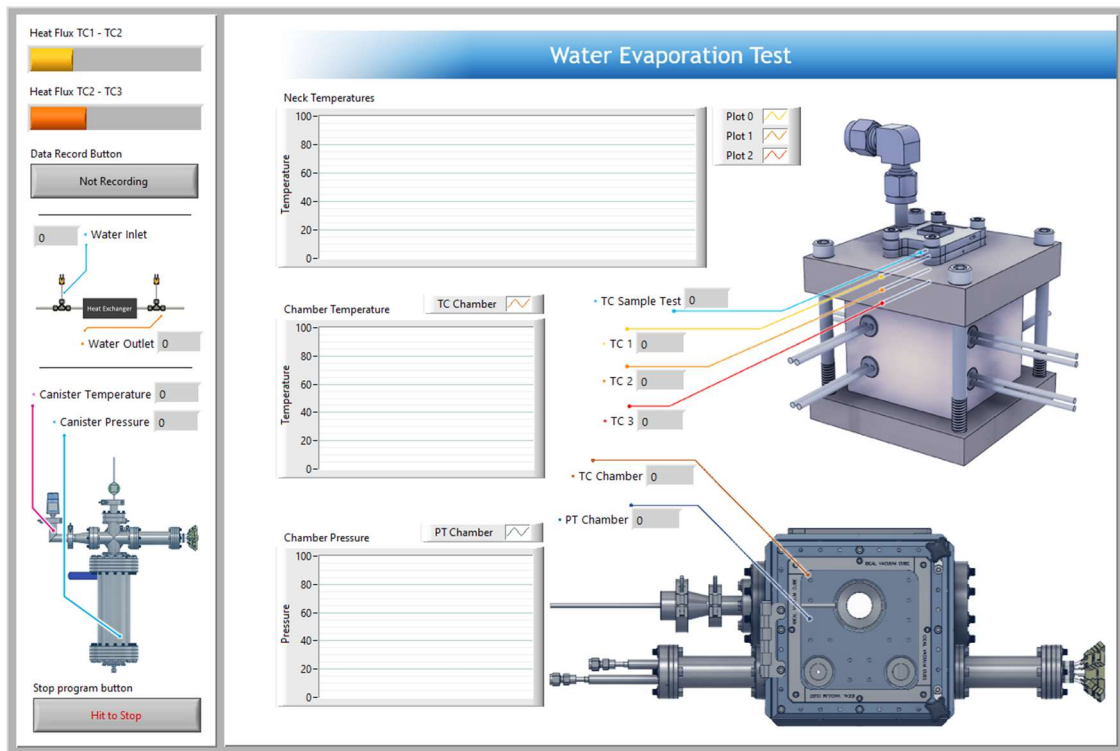


Figure 4-21: Thin film evaporation facility LabVIEW display.

4.2 Test Procedure

Initially, the fluid canister is filled with a known amount of water and sealed off to ensure no leaks are present. Pressure levels of the chamber and the canister were decreased to an ambient pressure of 3 kPa (22.5 Torr). Once desire pressure was reached, the fluid inside the canister was

heated using a rope heater that is wrapped around the exterior surface of the flange. Fluid was heated up to 60°C and temperature and pressure levels were displayed and monitored on the LabVIEW display. When the target temperature of the fluid was reached the manual valves on the main tubing line were opened to allow the fluid to flow throughout the line. Fluid transport was solely pressure driven by the differential in pressure between the fluid canister and the vacuum chamber. Fluid was cooled from 60°C to 24°C using a heat sink connected to a VARIAC power supply. The fluid temperature was monitored before and after entering the heat sink and the heat sinks fan speed was adjusted using the VARIAC power supply. Power level was determined based on active cooling of the fluid. The flow rate was adjusted using a low flow metering valve on the main tubing line before entering the chamber. Theoretical flow rate was determined based on expected heat flux and fluid properties. Fluid was then introduced into the sample and into the 1x1 cm² micropillar array by capillary action. Once thin film layer of the fluid was covering the micropillar array, the cartridge heaters on the evaporation assembly were powered on using a VARIAC power supply. Power was supplied to the heaters by gradual increments on the power supply dial position. Temperature readings of the copper neck, flat sample, and chamber were monitored on the LabVIEW display. System was allowed to reach steady state once gradual increase in power was supplied to the cartridge heaters. When temperature readings of the copper neck and the flat sample were not changing more than 0.5°C for 1 minute, data was recorded for 30 seconds. This gradual increasing in power was repeated until dry-out was seen on the micropillar sample resulting in the capillary limited dry-out heat flux. Temperature readings for each recorded data point were used to determine the heat flux of the sample. Data was processed and plotted to express the calculated heat flux as a function of the temperature difference of the test sample and the saturation temperature of the fluid.

4.3 Data Processing

Temperature readings throughout every test recording are averaged and were interpreted where heat flux was calculated from the following equation:

$$q'' = -k_{Cu} \frac{dT}{dx} \quad (18)$$

where k_{Cu} is the thermal conductivity of the copper heating block and $\frac{dT}{dx}$ is the temperature gradient along the copper neck defined by Cooke et al. (2011) shown in Eq. 19.

$$\frac{dT}{dx} = \frac{3T_1 - 4T_2 + T_3}{2\Delta x} \quad (19)$$

where T_1 , T_2 , and T_3 are the temperature readings of the copper block where T_1 is at the location closest to the test sample, and Δx is the spacing between the thermocouples, shown in Fig. 4-22.

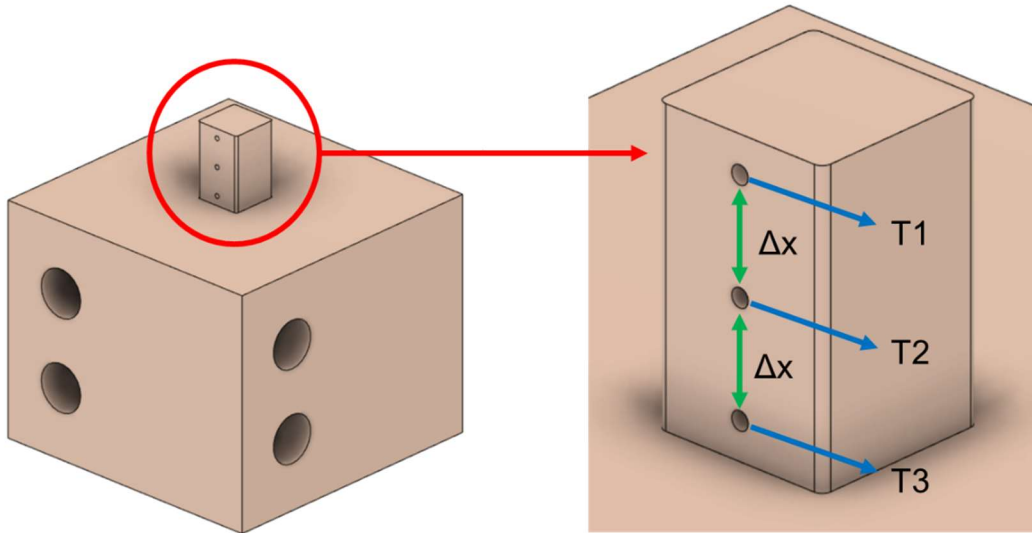


Figure 4-22: Zoomed view of thermocouple location along the neck of the copper heating block.

Calculated heat flux values for each test recording were determined and plotted against the temperature difference between the test sample heated surface and the saturation temperature at the testing conditions using Eq. 20.

$$\Delta T = T_4 - T_{sat} \quad (20)$$

where T_4 is the average test sample temperature for each recording and T_{sat} is the saturation temperature of water at the tested pressure conditions inside the chamber.

Plots were generated for each tested sample to express the calculated heat flux as a function of wall superheat. From the plots, critical heat flux (CHF) will be determined based on the trendline and heat flux values after dry-out is achieved.

Chapter 5: Thin Film Evaporation Results

5.1 Results and Discussion

Tests were performed on manufactured copper test samples with various micropillar dimensions to determine the dry-out heat flux and compare with the theoretical model calculated, shown in Fig. 5-1.

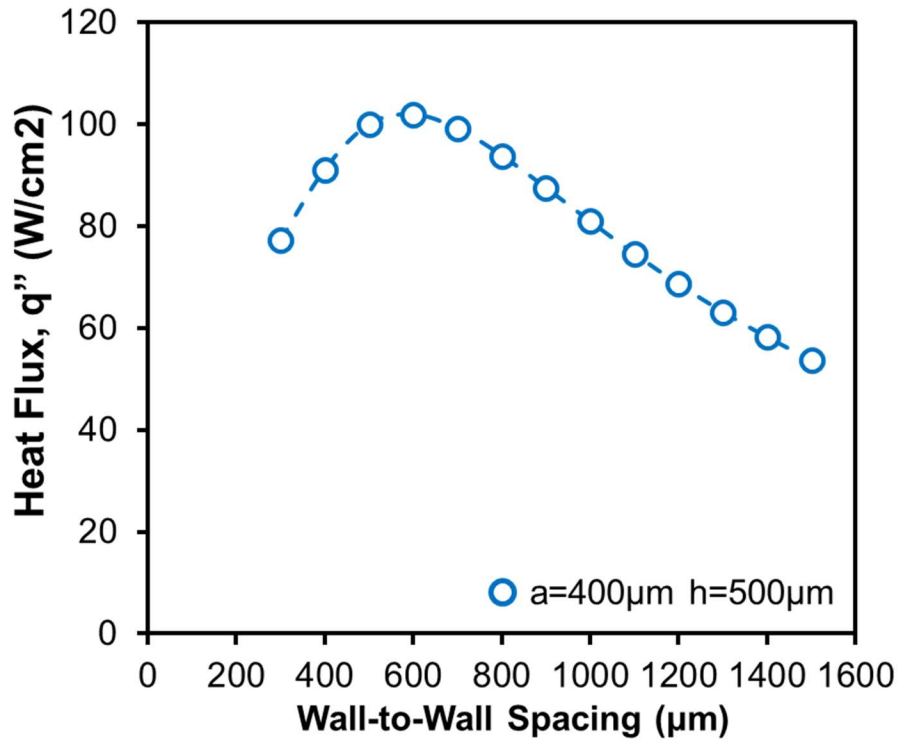


Figure 5-1: Theoretically calculated dry-out heat flux for manufactured copper samples.

Four different samples with different wall-to-wall spacing between micropillars and different micropillar height were tested to determine their heat transfer capabilities. Water entered the sample and onto the micropillar array by capillary action and a steady gradual increase in heat flux was applied until dry-out is achieved. Results for all four samples with known micropillar dimensions are shown.

5.1.1 Effect of Flow Rate

The first sample that was tested had known micropillar diameter of 400 μm , spacing of 500 μm , and height of 600 μm . As the test sample was subjected to gradual increases in heat, the sample surface temperature along with the three thermocouples placed on the copper heating block gradually increased. Initially, water entered the samples secondary reservoir making its way onto the four primary reservoirs and onto the 1x1 cm^2 micropillar array. As higher temperatures were reached, heat flux gradually increased as the temperature gradient between the thermocouples along the copper neck became more apparent. Initially, the test sample surface temperature is the same as the chamber temperature (25°C) at its respective saturation pressure (24 Torr). This ensured that water entering the sample was in fact at saturation conditions.

The effect of flow rate was determined by subjecting the sample to various flowrates of the working fluid onto the sample. This was done to determine when the dry-out heat flux becomes independent from the flow rate. This ensured that dry-out is indeed due to the super heat of the sample surface and not due to lack of liquid supply onto the sample. Fig. 5-2 presents the results from the thin film evaporation tests on the manufactured copper micropillar arrays. Y-axis presents the heat flux given to the micro-pillar arrays, and X-axis presents the wall-superheat that is the surface temperature above the water saturation temperature (here 24 °C). The different colors on the plot represent different tests performed at various flow rates on the same surface. The arrow represents the dry-out heat flux after which the heat flux goes down due to failure in liquid supply to the micro-structures through capillary action. A dry-out heat flux of $\sim 80 \text{ W/cm}^2$ was observed in the preliminary tests for the 500 μm conventional copper surface. However, the second test shows a slight decrease in dry-out point that is $\sim 76 \text{ W/cm}^2$.

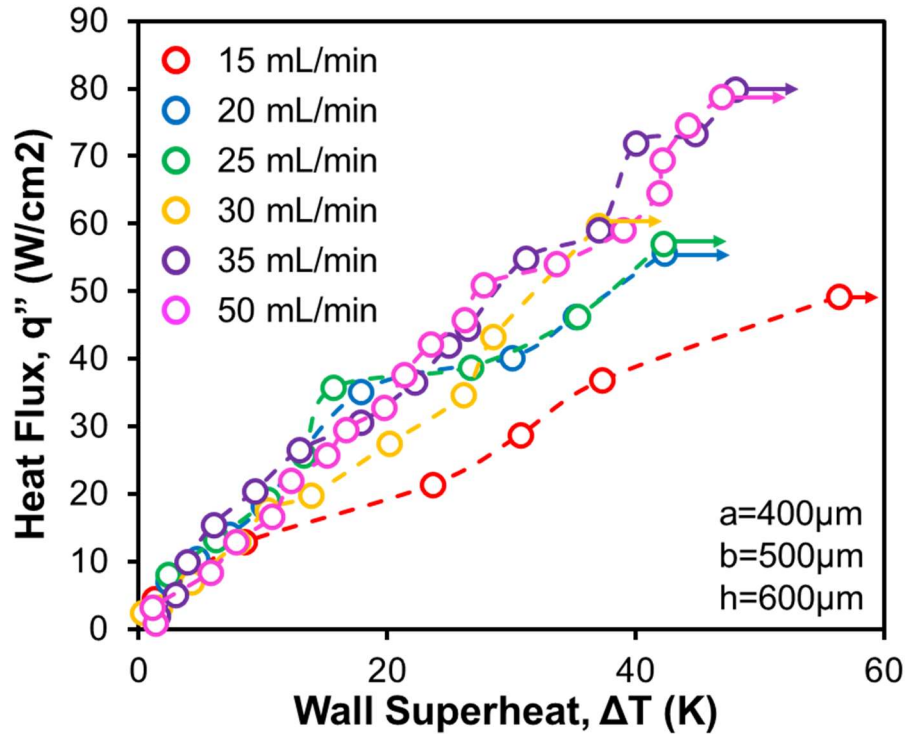


Figure 5-2: Heat flux as a function of surface superheat at various flow rates for copper sample $a=400\mu\text{m}$ $b=500\mu\text{m}$ $h=600\mu\text{m}$.

It was observed that between 35 mL/min and 50 mL/min heat flux becomes independent as similar heat flux values were obtained for these two flow rates. Due to the sample design, excess water is disposed once primary and secondary reservoirs are full. This confirmed that at these flow rates, dry-out heat flux is due to surface temperature superheat rather than fluid starvation on the samples reservoirs.

5.1.2 Effect of Micropillar Spacing

The effect of micropillar spacing on the dry-out heat flux was then determined. Three different samples with micropillars having known diameter of $400\mu\text{m}$ and height $500\mu\text{m}$ were

manufactured with various spacings of 500 μm , 800 μm , and 1100 μm . Once temperature readings along the assembly reached steady state conditions the first data point was recorded. Then, the VARIAC power supply that is connected to the assembly's cartridge heaters was then set to 5V supplying the first heat load to the copper heating block and onto the test sample. Data was recorded when the heat flux reading on the LabVIEW display would increase by 5 W/cm^2 . After determining the point where heat flux becomes independent of the flow rate a constant flow rate was set at a known position that supplies a flow rate of 50 mL/min. At higher heat loads, constant evaporation between the microstructures could be seen on the sample surface. Once partial dry-out at these evaporation sites occurred, water would wick back onto the micropillar array from the available fluid on the primary reservoirs. Heat flux plots for all three samples with different micropillar spacings is shown in Fig. 5-3.

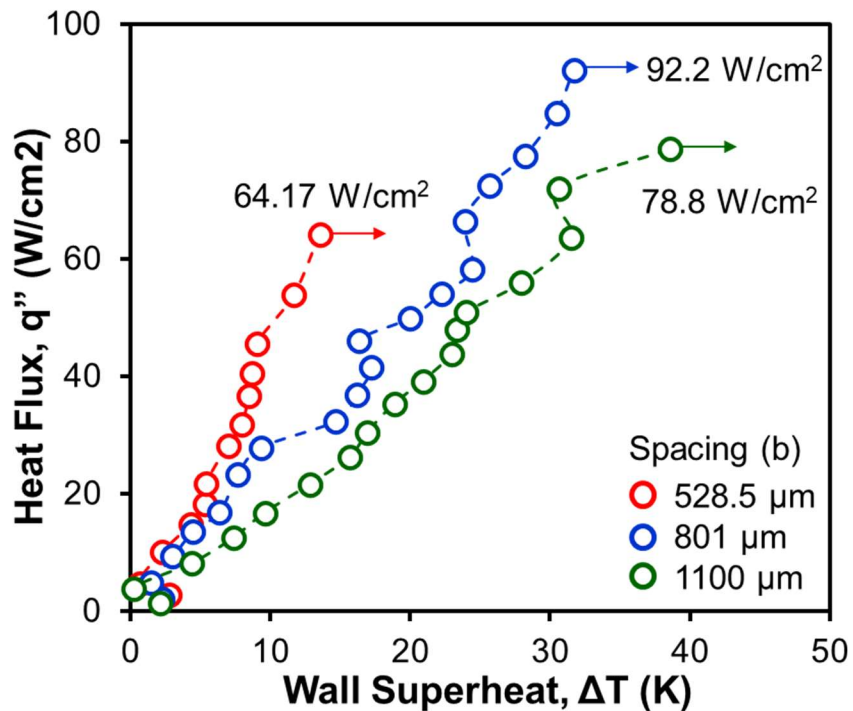


Figure 5-3: Heat flux as a function of surface superheat for copper samples having $a=400\mu\text{m}$ $h=500\mu\text{m}$ and various spacings at 50 mL/min.

For the sample having the smallest spacing, dry-out was seen at a wall superheat of 13.53°C and a heat flux of 64.17 W/cm². At this point, there was no active wicking onto the test sample micropillar array leading to the rapid increase in surface temperature. The dry-out was attributed to the surface temperature and not the lack of fluid supply as water continued to be dispatched from the secondary reservoir excess port.

The next sample tested had a wall-to-wall spacing of 800µm. Thin film evaporation was observed at a super heat of 17.23°C and a heat flux value of 41.5 W/cm². At dry-out, this sample was able to dissipate 92.2 W/cm² at a wall superheat of 31.7°C, the most heat removal from all tested samples.

The last sample tested was that with the largest spacing of 1100µm. As gradual increases in heat load were applied it could be seen that the sample surface temperature and on the plot that the slope changes slightly at 23.95°C and a heat flux of 50.8 W/cm². At this point there were many evaporation sites on the samples micropillar array as once partial dry-out occurred, water would wick onto the surface again forming the thin fluid layer along the wicking surface forming a meniscus allowing for thin film evaporation to occur. At a wall superheat of 38.56°C a critical heat flux of 78.7 W/cm² was achieved. It was at this point where water would not wick onto the surface due to the high temperature of the surface, resulting in the capillary limited dry-out heat flux.

5.2 Test Summary

Four manufactured copper samples with a 1x1cm² micropillar array were tested to determine their capillary limited dry-out heat flux at a constant flow rate of 50 mL/min. Samples were tested under a pressure of 24 Torr with its respective saturation temperature of 25°C. Heat fluxes ranging from 44.2 W/cm² to 92.2 W/cm² were achieved once the capillary limited dry-out

heat flux was achieved for various micropillar spacings and heights. Results show that the dry-out heat flux for each sample follows the predicted behavior established by the theoretical model. Fig. 5-4 shows the predicted dry-out heat flux as a function of intrinsic contact angle for two different angles. The experimental results are in good correlation with model for contact angle of 88° as a contact angle of 87° predicts 1.5 times more heat flux due to an increased capillary pressure with increasing contact angle. Capillary pressure is the driving force of the fluid onto the wicking surface, therefore, higher wicking leads to higher critical heat flux due to constant fluid supply to heated area.

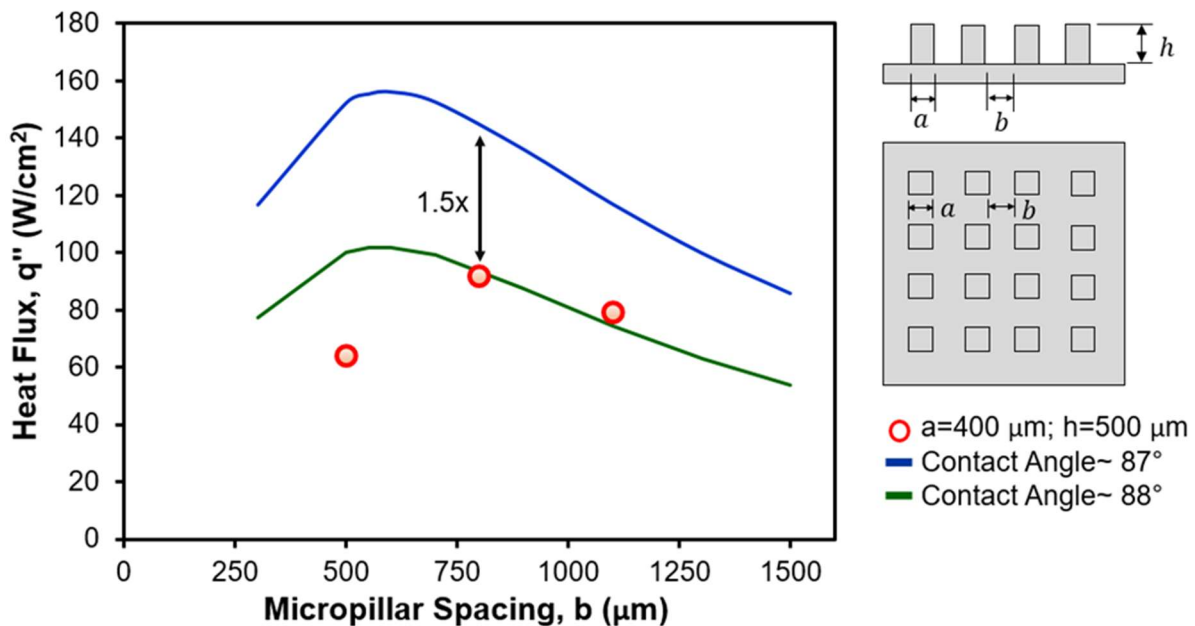


Figure 5-4: Theoretical model vs. experimental results for tested copper samples for different contact angles.

The two samples with same micropillar diameter and spacing of $400\mu\text{m}$ and $500\mu\text{m}$, respectively, but with different heights of $500\mu\text{m}$ and $600\mu\text{m}$ established that an increased micropillar height leads to a higher dry-out heat flux value. From the model, test sample with

800 μm wall-to-wall spacing was predicted to dissipate the most heat compared to the other samples. Experimental results showed that this sample was able to dissipate 92.2 W/cm², the highest of all tested samples. Three samples with the same height of 500 μm were manufactured to prove the theoretical plots trend showing that 800 μm is the optimum spacing for a copper-water application.

Lower experimental heat flux values are attributed to the surface roughness of the manufactured samples along with certain fabrication and manufacturing errors leading to lower or higher values for the proposed micropillars. Higher surface roughness leads to more sites for nucleation which leads to lower the heat flux values using thin film evaporation. Studies done by Kim et al. (2018) have shown that increasing surface roughness along with the contact angle led to a decrease in heat flux compared to smoother surfaces. For pool boiling, more nucleation sites are desired to for better thermal performance while in thin film evaporation it is key to avoid nucleation and solely depend on the evaporation of the fluid meniscus. Chan et al. (2009) investigated the performance of a finned surface using pool boiling in low vapor pressures. Fins having a wall-to-wall spacing of 500 μm and height of 15mm were able to dissipate about 65W/cm². In comparison, structures that were tested in this work are 30 times smaller and can achieve similar heat fluxes, proving that thin film evaporation with the use of micropillars is a smaller scale efficient cooling strategy.

Samples with 500 μm wall-to-wall spacing show the lowest value of dry-out heat flux due to low permeability and capillary pressure which is dependent on the contact angle. Capillary pressure is proportional to micropillar dimensions along with the contact angle of water on a copper surface, therefore a larger contact angle leads to lower heat flux. Sample having a spacing of 800 μm , dissipated the most heat due to high permeability and capillary pressure. Capillary

pressure is the driving force of fluid onto the micropillar array, therefore maximum pressure is desired.

Thin film evaporation results were then compared to past work done, shown in Fig. 5-5. Experimental results were plotted as a function of width-to-spacing ratio as previous work done by Solomon et al. and Farokhnia et al. had smaller scale micropillar arrays compared to this work. The plot shows that the manufactured test samples presented in this work can dissipate higher heat fluxes with larger scale micropillars with small width-to-spacing ratios.

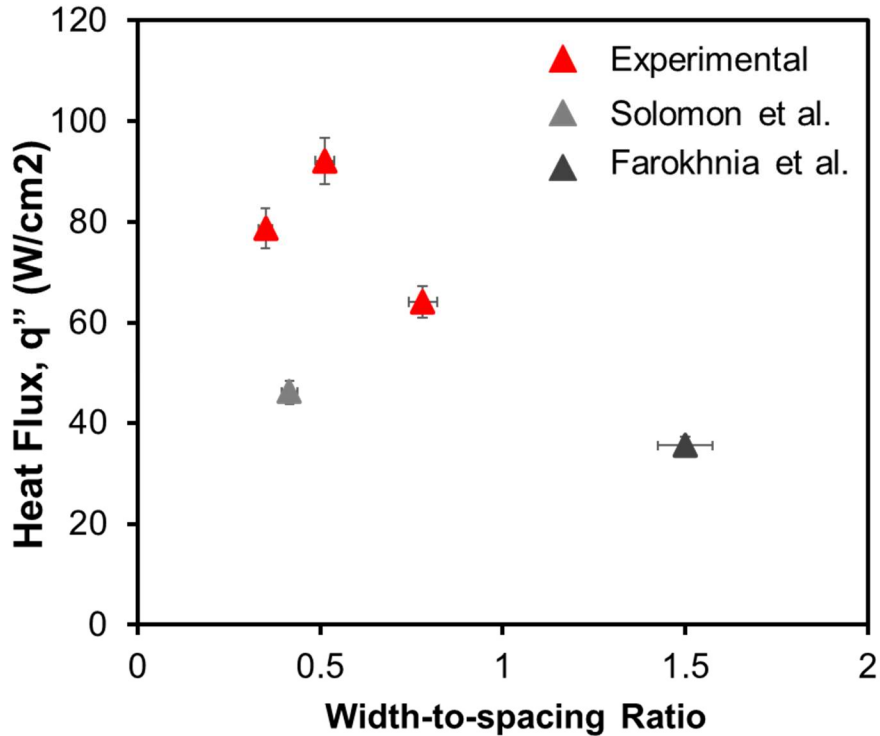


Figure 5-5: Experimental results compared to work done by Solomon et al. and Farokhnia et al.

Future work for this thin film evaporation test facility includes improving the thermal contact between for the use of titanium samples. This will result in better thermal performance and

the test sample will be able to dissipate higher heat fluxes. Although titanium has relatively low thermal conductivity and is hard to machine, it provides a great solution for high temperature applications due to its high compressive and tensile stress, fracture toughness oxidation resistance and high strength-to-weight ratio (Yuan et al. 2021).

Chapter 6: Conclusion

Conventionally manufactured copper surfaces with known micropillar dimensions were tested to determine their heat transfer capabilities. SEM images of the test surfaces showed the actual dimensions of these surfaces which were used to theoretically predict the dry-out heat flux for each surface. The theoretical model was adapted from Solomon et al. (2016) which accounts for micropillar dimensions, intrinsic contact angle, and fluid properties. Solid to fluid interactions are the driving force for constant heat dissipation of these surface, therefore it is crucial to understand the relation these parameters have on the capillary limited dry-out heat flux. The lower the intrinsic contact angle, the less the value for the expected heat flux is as capillary pressure is dependent on the contact angle which is the driving force of the fluid onto the wicking surface. Experimental results showed good correlation with the expected theoretical values for known micropillar spacings. Manufactured sample with the smallest wall-to-wall spacing between micropillars dissipated 64.17 W/cm^2 , the least of all test surfaces, while the sample with $800 \mu\text{m}$ spacing was able to remove the most heat from all samples, a dry-out heat flux of 92.2 W/cm^2 . Experimental results were compared with previous studies done on smaller scale manufactured surfaces. The width-to-spacing ratio was considered due to this work exploring larger scale microstructures. Results obtained in this work show higher critical heat fluxes at a lower width-to-spacing ratios proving effective heat transfer at larger scale microstructures.

References

- Adera, Solomon. "Thin-Film Evaporation from Well-Defined Silicon Micropillar Wicks for High Heat Flux Thermal Management." Thesis, Massachusetts Institute of Technology, 2016.
- Adera, Solomon, Dion Antao, Rishi Raj, and Evelyn N. Wang. "Design of Micropillar Wicks for Thin-Film Evaporation." *International Journal of Heat and Mass Transfer* 101 (2016): 280–94. <https://doi.org/10.1016/j.ijheatmasstransfer.2016.04.107>.
- Anderson, W. G., P. M. Dussinger, D. B. Sarraf, and S. Tamanna. "Heat Pipe Cooling of Concentrating Photovoltaic Cells." *2008 33rd IEEE Photovoltaic Specialists Conference*, 2008. <https://doi.org/10.1109/pvsc.2008.4922577>.
- Chan, Mark Aaron, Christopher R. Yap, and Kim Choon Ng. "Pool Boiling Heat Transfer of Water on Finned Surfaces at near Vacuum Pressures." *Journal of Heat Transfer* 132, no. 3 (2009). <https://doi.org/10.1115/1.4000054>.
- Chaudhry, Hassam Nasarullah, Ben Richard Hughes, and Saud Abdul Ghani. "A Review of Heat Pipe Systems for Heat Recovery and Renewable Energy Applications." *Renewable and Sustainable Energy Reviews* 16, no. 4 (2012): 2249–59. <https://doi.org/10.1016/j.rser.2012.01.038>.
- Cooke, Dwight, and Satish G. Kandlikar. "Pool Boiling Heat Transfer and Bubble Dynamics over Plain and Enhanced Microchannels." *Journal of Heat Transfer* 133, no. 5 (May 2011): 1–9. <https://doi.org/10.1115/1.4003046>.
- Farokhnia, Nazanin, Peyman Irajizad, Seyed Mohammad Sajadi, and Hadi Ghasemi. "Rational Micro/Nanostructuring for Thin-Film Evaporation." *The Journal of Physical Chemistry C* 120, no. 16 (2016): 8742–50. <https://doi.org/10.1021/acs.jpcc.6b01362>.
- Hauner, Ines M., Antoine Deblais, James K. Beattie, Hamid Kellay, and Daniel Bonn. "The Dynamic Surface Tension of Water." *The Journal of Physical Chemistry*, March 16, 2017, 1599–1603. <https://doi.org/10.1021/acs.jpcclett.7b00267.s001>.
- Hayat, Muhammad Aamer, Hafiz Muhammad Ali, Muhammad Mansoor Janjua, William Pao, Changhe Li, and Mostafa Alizadeh. "Phase Change Material/Heat Pipe and Copper Foam-Based Heat Sinks for Thermal Management of Electronic Systems." *Journal of Energy Storage* 32 (2020): 101971. <https://doi.org/10.1016/j.est.2020.101971>.
- Ivanova, Mariya, Yvan Avenas, Christian Schaeffer, Jean-Bernard Dezord, and Juergen Schulz-Harder. "Heat Pipe Integrated in Direct Bonded Copper (DBC) Technology for Cooling of Power Electronics Packaging." *IEEE Transactions on Power Electronics* 21, no. 6 (2006): 1541–47. <https://doi.org/10.1109/tpel.2006.882974>.

- Kim, Jin S., Adam Girard, Seongchul Jun, Jungho Lee, and Seung M. You. “Effect of Surface Roughness on Pool Boiling Heat Transfer of Water on Hydrophobic Surfaces.” *International Journal of Heat and Mass Transfer* 118 (2018): 802–11. <https://doi.org/10.1016/j.ijheatmasstransfer.2017.10.124>.
- Korson, Lawrence, Walter Drost-Hansen, and Frank J. Millero. “Viscosity of Water at Various Temperatures.” *The Journal of Physical Chemistry* 73, no. 1 (1969): 34–39. <https://doi.org/10.1021/j100721a006>.
- Li, Ji, and Lucang Lv. “Experimental Studies on a Novel Thin Flat Heat Pipe Heat Spreader.” *Applied Thermal Engineering* 93 (2016): 139–46. <https://doi.org/10.1016/j.applthermaleng.2015.09.038>.
- MONTEITH, J. L. “Latent Heat of Vaporization in Thermal Physiology.” *Nature New Biology* 236, no. 64 (1972): 96–96. <https://doi.org/10.1038/newbio236096a0>.
- Orlova, E G, D V Feoktistov, and K A Batishcheva. “Dynamic Contact Angle and Three-Phase Contact Line of Water Drop on Copper Surface.” *IOP Conference Series: Materials Science and Engineering* 93 (2015): 012010. <https://doi.org/10.1088/1757-899x/93/1/012010>.
- Orlova, Evgenija, Dmitriy Feoktistov, and Geniy Kuznetsov. “Investigation of Drop Dynamic Contact Angle on Copper Surface.” *EPJ Web of Conferences* 82 (2015): 01053. <https://doi.org/10.1051/epjconf/20158201053>.
- Plawsky, J. L., A. G. Fedorov, S. V. Garimella, H. B. Ma, S. C. Maroo, L. Chen, and Y. Nam. “Nano- and Microstructures for Thin-Film Evaporation—a Review.” *Nanoscale and Microscale Thermophysical Engineering* 18, no. 3 (2014): 251–69. <https://doi.org/10.1080/15567265.2013.878419>.
- Ranjan, Ram, Jayathi Y. Murthy, and Suresh V. Garimella. “A Microscale Model for Thin-Film Evaporation in Capillary Wick Structures.” *International Journal of Heat and Mass Transfer* 54, no. 1-3 (2011): 169–79. <https://doi.org/10.1016/j.ijheatmasstransfer.2010.09.037>.
- Ranjan, Ram, Jayathi Y. Murthy, and Suresh V. Garimella. “Analysis of the Wicking and Thin-Film Evaporation Characteristics of Microstructures.” *Journal of Heat Transfer* 131, no. 10 (2009). <https://doi.org/10.1115/1.3160538>.
- Sangani, A.S., and A. Acrivos. “Slow Flow Past Periodic Arrays of Cylinders with Application to Heat Transfer.” *International Journal of Multiphase Flow* 8, no. 3 (1982): 193–206. [https://doi.org/10.1016/0301-9322\(82\)90029-5](https://doi.org/10.1016/0301-9322(82)90029-5).
- Shukla, K. N. “Heat Pipe for Aerospace Applications—an Overview.” *Journal of Electronics Cooling and Thermal Control* 05, no. 01 (2015): 1–14. <https://doi.org/10.4236/jectc.2015.51001>.

- Tanaka, M, G Girard, R Davis, A Peuto, and N Bignell. "Recommended Table for the Density of Water between 0 °C and 40 °C Based on Recent Experimental Reports." *Metrologia* 38, no. 4 (2001): 301–9. <https://doi.org/10.1088/0026-1394/38/4/3>.
- Wang, Yaxiong, and G. P. Peterson. "Investigation of a Novel Flat Heat Pipe." *Journal of Heat Transfer* 127, no. 2 (2005): 165–70. <https://doi.org/10.1115/1.1842789>.
- Xiao, Rong, Ryan Enright, and Evelyn N. Wang. "Prediction and Optimization of Liquid Propagation in Micropillar Arrays." *Langmuir* 26, no. 19 (2010): 15070–75. <https://doi.org/10.1021/la102645u>.
- Yekta-fard, M., and A. B. Ponter. "Surface Treatment and Its Influence on Contact Angles of Water Drops Residing on Teflon and Copper." *The Journal of Adhesion* 18, no. 3 (1985): 197–205. <https://doi.org/10.1080/00218468508079683>.
- Yuan, Chua Guang, A. Pramanik, A. K. Basak, C. Prakash, and S. Shankar. "Drilling of Titanium Alloy (Ti6Al4V) – A Review." *Machining Science and Technology* 25, no. 4 (2021): 637–702. <https://doi.org/10.1080/10910344.2021.1925295>.
- Zhu, Yangying. "Micro and Nanostructures for Two-Phase Fluid and Thermal Transport," 2017.

Vita

Alejandro Amador is born and raised in El Paso, Texas where he graduated from Horizon High School in 2016. After obtaining his high school diploma and receiving a presidential scholarship to the University of Texas at El Paso (UTEP) he enrolled to pursue a Bachelor of Science in Mechanical Engineering. During his undergraduate studies, Alejandro was part of the VTOL research group at the Center for Space Exploration and Technology Research where he studied the incorporation of a fully additively manufactured aircraft that can take flight and release a payload while in the air. He then would perform his senior design studies in collaboration with Lockheed Martin Collaborative Human Immersive Laboratory (CHIL) to develop a virtual reality haptic suit that simulates real life space missions in a virtual environment.

After obtaining his Bachelor of Science in Mechanical Engineering degree in December of 2019, Alejandro was admitted into the UTEP graduate school to pursue a Master of Science in Mechanical Engineering. Alejandro then obtained a position as a graduate research assistant at the Aerospace Center at UTEP. In the 2 years as a research assistant, Alejandro was part of multiple research teams where he explored in-situ resource utilization (ISRU) of water on the lunar surface along with thermal mining technologies. Additionally, Alejandro experimentally characterized the critical heat flux and minimum film boiling heat flux for additively manufactured cooling channels for liquid nitrogen saturated flow boiling in collaboration with NASA Marshall Space Flight Center. He concluded his graduate research with the UTEP Hypersonics team where he studied the thin film evaporation of water for high heat flux applications through the Air Force Research Laboratory through the National Center for Defense Manufacturing and Machining.

After graduating with his master's degree, Alejandro joined Lockheed Martin Aeronautics as an Electro-Optical Systems Engineer.